

The Impact of Aerosols on the Stratiform Clouds over Southern West Africa: A Large-Eddy Simulation Study

Lambert Delbeke¹, Chien Wang¹, Pierre Tulet¹, Cyrielle Denjean², Maurin Zouzoua³, Nicolas Maury⁴
5 and Adrien Deroubaix⁵

¹Laboratoire d'Aérodynamique, Université de Toulouse, CNRS, UT3, IRD, Toulouse, France

²CNRM, Université de Toulouse, Météo-France, CNRS, Toulouse, France

³Laboratoire Atmosphères, Milieux, Observations Spatiales, IPSL, CNRS, Guyancourt, France

⁴CNRM, Université de Toulouse, Météo-France, CNRS, Toulouse; now at LMD/IPSL, Paris, France

10 ⁵IUP, Institute of Environmental Physics, University of Bremen, Bremen, and Max Plank Institute for Meteorology, Hamburg, Germany

Correspondence to: Chien Wang (chien.wang@aero.obs-mip.fr), Cyrielle Denjean (cyrielle.denjean@meteo.fr)

Abstract. The low level stratiform clouds (LLSCs) covering a large area appear frequently during the wet monsoon season in southern West Africa. This region is also a place where different types of aerosols
15 coexist, including the biomass burning aerosols coming from Central and South Africa and the aerosols emitted by local anthropogenic activities. We investigate the indirect and semi-direct effects of these aerosols on the life cycle of LLSCs by conducting a case study based on the airborne and ground-based observations from the field campaign of Dynamic-Aerosol-Chemistry-Cloud-Interaction in West Africa (DACCIWA). This case is modeled using a Large Eddy Simulation (LES) model with fine resolution and
20 in-situ aerosol measurements including size distribution and chemical composition. The model has successfully reproduced the observed life cycle of the LLSC, from stratus formation to stabilization during the night, and to the upward development after sunrise until break-up of cloud deck in the late afternoon. Additional sensitivity simulations using different measured aerosol profiles also suggest that aerosols can affect the cloud life cycle through both the indirect and semi-direct effect. As expected,
25 modeled cloud microphysical features including cloud droplet number concentration, mean radius, and thus cloud reflectivity are all controlled by aerosol concentration. However, it is found that the difference in cloud reflectivity is not always the only factor in determining the variation of the incoming solar radiation at ground and cloud life cycle after sunrise. Instead, the difference in cloud fraction brought by dry air entrainment from above and thus the speed of consequent evaporation - also influenced by aerosol
30 concentration, is another important factor to consider. Clouds influenced by higher aerosol concentrations and thus having higher number concentration and smaller sizes of cloud droplets are found to evaporate more easily and thus impose a lower cloud fraction. In addition, we find that an excessive atmospheric heating up to $12 K day^{-1}$ produced by absorbing black carbon aerosols (BC) in our modeled cases can lower the height of cloud top and liquid water path, resulting a weaker extent in vertical development
35 while a higher cloud fraction, delaying intense cloud break-up until later afternoon, making a positive contribution to the indirect effect. While the resulted thinner clouds from such a heating, on the other hand, would break up faster in late afternoon, thus contributing negatively to the indirect effect.

1. Introduction

40 Low-level stratiform clouds (LLSCs) have a higher albedo and a larger cloud deck covering Earth's surface than many other types of clouds (Hartmann *et al.*, 1992; Chen *et al.*, 2000; Eastman and Warren, 2014). Their reflection of solar radiation is thus important to Earth's radiative budget. LLSCs often occupy the upper few hundred meters in the planetary boundary layer (PBL), and their persistent appearance relies on a stable PBL that is normally associated with a large-scale subsidence above because
45 of a high-pressure system. These clouds are often formed over cooler subtropical and mid-latitude oceans, constantly covering more than 50% of these areas (Wood, 2012). During the West African monsoon season, LLSCs frequently form over continental southern West Africa (SWA) in the night and usually break up in the early afternoon of the following day (Schrage and Fink, 2012; Schuster *et al.*, 2013). Under a polluted condition, LLSCs are characterized by numerous and small cloud droplets, increasing
50 the cloud albedo, suppressing drizzle, and extending the cloud lifetime (Twomey, 1957; Haywood and Boucher, 2000; Liu *et al.*, 2014; Carslaw *et al.*, 2017). The presence of LLSCs impacts on the radiative budget of the atmosphere, surface fluxes, the diurnal cycle of the convective boundary layer, and thus the regional climate (Knippertz *et al.*, 2011; Hannak *et al.*, 2017). However, the diurnal cycle of LLSCs is still poorly represented in weather and climate models, especially over SWA, because the processes
55 behind the variability of LLSCs cover remain elusive (Knippertz *et al.*, 2011; Hannak *et al.*, 2017; Hill *et al.*, 2018).

Stratiform clouds are sensitive to aerosol concentration, chemical composition, and vertical distribution. This is because that aerosol can directly scatter or absorb solar radiation (the direct effect or aerosol-radiation effect), or by serving as cloud nuclei, influence cloud microphysical structure and thus
60 reflectance or lifetime (the indirect aerosol effects or radiative effect of aerosol-cloud interaction plus cloud adjustment) (Boucher *et al.*, 2013). The heating associated with aerosol absorption of solar radiation would be able to perturb atmospheric thermodynamic stability and thus dynamical processes as well (the semi-direct effect) (Hansen *et al.*, 1998). Such a semi-direct effect can be positive or negative depending on the relative distribution of the aerosol with respect to clouds (*e.g.*, Johnson *et al.*, 2004;
65 Feingold *et al.*, 2005). All these effects can modify the energy budget and thus the status of the planetary boundary layer where the stratiform clouds form and evolve. Aerosols inside stratiform clouds can also be modified by aqueous physio-chemical processes (Wood, 2012). Interactions between aerosols and clouds, and their effects on radiation, precipitation, and regional circulations, remain one of the largest uncertainties in understanding and projecting climate change. Indeed, the indirect effect of aerosol is still
70 difficult to estimate (Boucher *et al.*, 2013). Climate models struggle to minimize such uncertainties (Li *et al.*, 2022). Several previous studies were conducted to investigate aerosol-clouds interactions in LLSCs using high-resolution Large-Eddy Simulation (LES) models, though mainly on cases over ocean (*e.g.*, Ackerman *et al.*, 2004; Sandu *et al.*, 2008; Twohy *et al.*, 2013; Flossmann and Wobrock, 2019), where surface fluxes often have insignificant diurnal variation and latent heat alongside moisture from
75 evaporation at sea surface dominate, differing from the cases over land (Wood, 2012; Ghonima *et al.*, 2014).

During the West Africa Monsoon (WAM), aerosols can come from both local and remote sources to SWA. A large amount of Biomass Burning Aerosols (BBA) can be transported from southern and Central African towards SWA during the summer monsoon (Haslett *et al.*, 2019). These air masses are also

80 loaded with additional aerosols from anthropogenic emissions upon reaching the highly urbanized
regions near the coast (Chatfield *et al.*, 1998; Sauvage *et al.*, 2005; Mari *et al.*, 2008; Murphy *et al.*, 2010;
Reeves *et al.*, 2010; Menut *et al.*, 2018; Haslett *et al.*, 2019). A significant quantity of wind-blown mineral
dust aerosols emitted from the Sahara and Sahel throughout the year with a peak in springtime
85 (Marticorena and Bergametti, 1996) can also reach SWA, often in June (Knippertz *et al.*, 2017). Local
sources of aerosols in SWA are related to anthropogenic activities near the coast, from where polluted
plumes would transport inland (Deroubaix *et al.*, 2019). These emissions are projected to increase with
the expected growth of the population (Lioussé *et al.*, 2014). Different emission sources also lead to a
complex mix of aerosol constituents in the aera, having a serious impact on human health (Bauer *et al.*,
2019), and possibly complicating the aerosol impacts on the diurnal cycle of LLSCs as well as
90 precipitation over SWA (Taylor *et al.*, 2019).

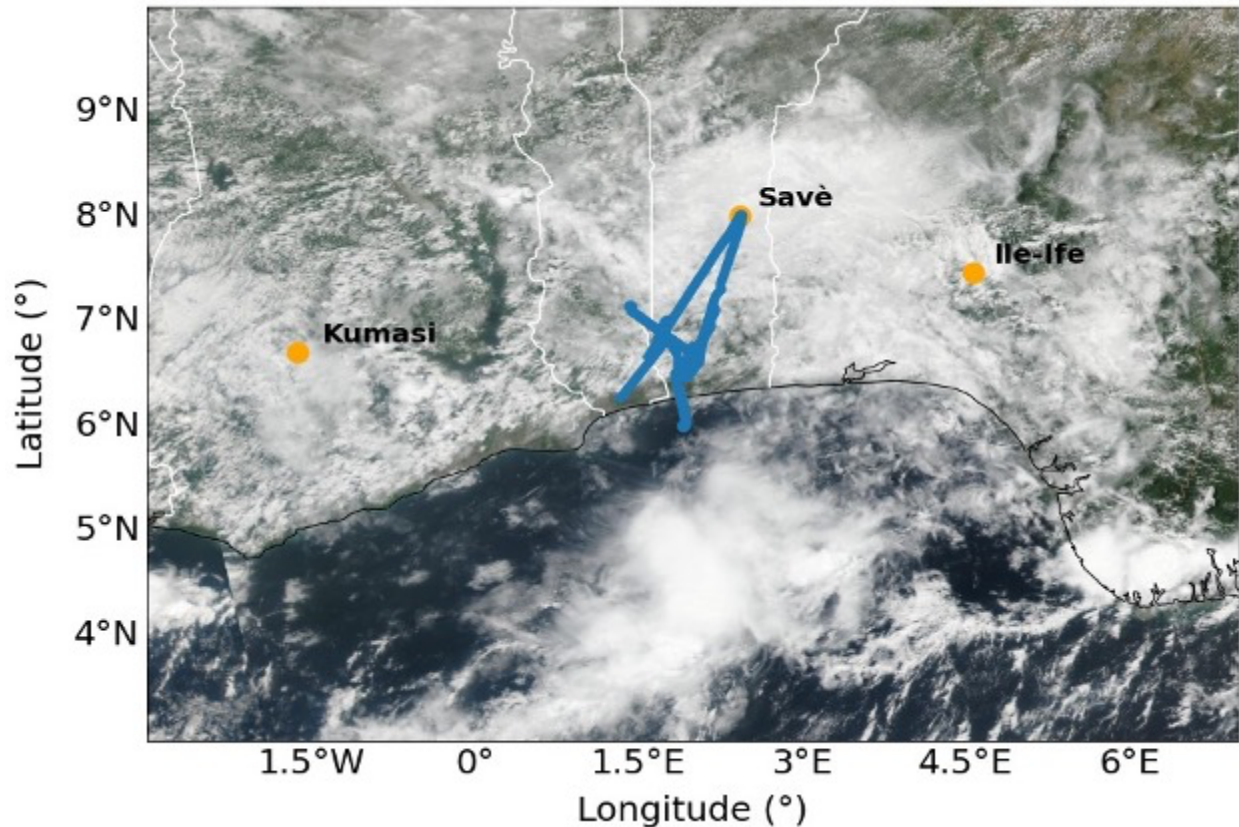


Figure 1. Map of southern West Africa with Savè, Kumasi and Ile-Ife locations and the flight track (blue line) of the ATR-42 the 3 July 2016 with NASA Suomi NPP/VIIRS true color corrected reflectance (<https://worldview.earthdata.nasa.gov/>).

95 The DACCIWA project was designed to better characterize cloud-aerosol-precipitation interactions
in SWA (Knippertz *et al.*, 2015). The measurement campaign conducted in June-July 2016 has provided
a comprehensive set of ground-based and airborne measurements of clouds and aerosols (Knippertz *et al.*,
et al., 2017; Kalthoff *et al.*, 2018; Flamant *et al.*, 2018) and inspired model analyses. The measurements

were conducted at three supersites, Savè (Benin), Kumasi (Ghana) and Ile-Ife (Nigeria) (Fig.1) and coordinated with three research aircrafts: the French ATR-42 operated by SAFIRE (Service des Avions Français Instrumentés pour la Recherche en Environnement), the British Twin Otter operated by British Antarctic Survey, and the German Falcon aircraft operated by DLR (Deutsches Zentrum für Luft und Raumfahrt). Additional radiosoundings were launched from Savè with high temporal frequency, which specifically benefits the monitoring of the LLSCs diurnal evolution.

Based on observations and a parcel model, Taylor *et al.* (2019) and Denjean *et al.* (2020a) showed that most cloud condensation nuclei and absorbing aerosols observed during DACCWA campaign were from ubiquitous long-range transported BBA, causing a polluted background which limits the effect of local pollution on cloud properties and aerosol radiative effects. Using COSMO-ART model in a simulation for 2-3 July 2016 case, Deetz *et al.* (2018) found that under the influence of the Maritime Inflow (MI, cold air) from Guinean Gulf, stratus-stratocumulus transition is susceptible to the aerosol direct effect, resulting in a spatial shift in the MI front and a temporal shift of the cloud transition. Over SWA and influenced by anthropogenic emission sources, the break-up time of LLSCs can be delayed by one hour and daily precipitation rate can decrease by 7.5% according to Deroubaix *et al.* (2022). Moreover, the semi-direct and indirect effects of aerosol were also studied together by varying respective magnitude or emissions of anthropogenic aerosols, though not being examined separately. Haslett *et al.* (2019) indicated that cloud droplets number concentration could increase up to 27 % due to transported BBA using COSMO-ART, making cloud and rain less sensitive to further increase in regional anthropogenic emissions. The impact of sedimentation on LLSCs has been studied by Dearden *et al.* (2018) using the Met Office NERC Cloud model (MONC) who demonstrated that sedimentation of cloud droplets, determined by droplet size, could affect liquid water path by removing droplets from the entrainment zone, or by lowering the cloud base and creating more heterogeneous cloud structure. Menut *et al.* (2019) showed with WRF-CHIMERE that a decrease of anthropogenic emissions along the SWA coast led to a northward shift of the monsoonal precipitation and the increase of surface wind speed over arid region in the Sahel, resulting in an increase of mineral dust emission. These previous modeling studies all highlighted in a regional scale while considering only limited aerosol chemical compositions rather than all aerosol species particularly black carbon (BC) measured during the field campaign. Pedruzo-Bagazgoitia *et al.* (2020) analyzed the stratocumulus-cumulus transition at a fine scale (a dozen of kilometer sidelong) using a LES at high resolution (50x50 m²), though aerosol effects were not being taken into consideration.

The aim of this study is to understand the specific impacts of local and transported aerosols on the life cycle of LLSCs during the monsoon period over SWA. In doing so, observational data obtained from the well-documented DACCWA field campaign have been used to constrain a high-resolution LES model including an interactive aerosol module that is able to represent the complex aerosol compositions. This modeling effort is also among a few studies that model and analyze stratiform cloud diurnal cycle over land rather than ocean. A description of observations, data, and the model as well as configurations of different simulations will be presented in the Method section after the Introduction. Then the results of an analysis aiming to understand and validate the modeled reference case against measurements will be discussed. Thereafter, the results from several sensitivity simulations will be presented. These sensitivity simulations use various observed aerosol profiles with different size distributions and chemical

140 compositions, designed to examine the indirect and semi-direct effects of aerosols on the life cycle of modeled LLSCs. This makes the analysis the first such modeling attempt within the framework of DACCIWA campaign. The last section of the paper will summarize major research findings of this study.

2. Methods

145 2.1 Observational data

We have used certain measurements of the DACCIWA field campaign to select our LLSC case and to configure the model simulations. These data are described as follows.

i) Radiosonde data: During DACCIWA campaign, radiosondes were launched with the MODEM system every 1 to 1.5 hour between 17:00 and 11:00 UTC (the local time of Benin is UTC+1) at the supersite of Savè in Benin. This site is located 185 km from the coast and 166 m above sea level. The area is rather flat, and the vegetation is mainly composed of small trees and shrubs. Temperature, pressure, relative humidity, and wind vertical profiles below 1500 m above ground level were measured with a 1 s temporal interval (4 - 5 m of vertical resolution) (Derrien *et al.*, 2016). These sondes were obtained using two balloons of different volumes to reach a preset time of ascent, and after the cutting of the larger balloon, the second one would be used to retrieve the sonde for another use (Legain *et al.*, 2013).

ii) Ground-based measurements: At the supersite of Savè, a CHM15k Ceilometer was deployed by the Karlsruher Institut für Technologie (KIT) to measure the cloud base height continuously with a 1 min interval and a 15 m vertical resolution, based on the backscatter profiles produced by the lidar with a wavelength of 1064 nm and a 5-7 kHz rate (Handwerker *et al.*, 2016). The cloud cover was monitored every day by using a MOBOTIX S15 cloud camera, installed by Université Paul Sabatier (UPS) team, to obtain pictures in visible and IR every 2 min. The aperture angles for the IR channel corresponds to a 158 m x 114 m area at a height of 200 m and pictures are coded in RGB components. A microwave radiometer (humidity and temperature profiler HATPRO-G4 from Radiometer Physics GmbH) was installed by KIT to measure brightness temperature to retrieve absolute humidity, liquid water path, and air temperature. The surface heat and radiation fluxes were measured with an energy balance station deployed over grass and bushes. Additional measurements include soil heat flux, air density, and turbulence parameters.

iii) Airborne measurements: The aircraft campaign took place from 29 June to 16 July 2016, conducted collaboratively by three research aircraft. In this study, only data from the ATR-42 were used as it flew around Savè between 10:00 and 11:00 UTC and probed the cloud layer. The cloud droplet size distribution was measured with a cloud droplet probe (CDP) (Taylor *et al.*, 2019). The chemical composition for non-refractive compounds was measured with the Aerodyne compact Time-of-Flight Aerosol Mass Spectrometer (HR-ToF-AMS) (Brito *et al.*, 2018). The black carbon (BC) mass concentration was measured with a single particle soot photometer (SP2) (Denjean *et al.*, 2020b). The aerosol size distribution was measured with a custom-built scanning mobility sizer spectrometer (SMPS, 20–485 nm), an ultra-high sensitivity aerosol spectrometer (UHSAS, 0.04–1 μm), and an optical particle counter (OPC GRIMM model 1.109, 0.3–32 μm) corrected for the complex refractive index provided in Denjean *et al.* (2020a). The total number concentration of particles larger than 10 nm was measured by a condensation particle counter (CPC, model MARIE). Meteorological variables such

as temperature, humidity, pressure, and wind speed and direction were also measured by a suite of airborne instruments. A gas concentration analyzer was used to measure certain chemical gases including CO₂, CH₄, and CO.

185 2.2 Description of the studied case

Our study analyzes the diurnal cycle of LLSCs based on the observed case of 3 July 2016 at the Savè supersite (Fig. 2). The cloud deck formed during the night, at around 02:00 UTC, close to the appearance of the core Nocturnal-Low-Level Jet (NLLJ), which could have a maximum speed around 6 m s⁻¹ (Kalthoff *et al.*, 2018), associated with a maximum cooling (Lohou *et al.*, 2020). At formation, the cloud base and top heights were located around 310 ± 30 m and 640 ± 100 m, respectively, and were maintained
 190 due to the cloud top radiative cooling and cold advection (Dione *et al.*, 2019).

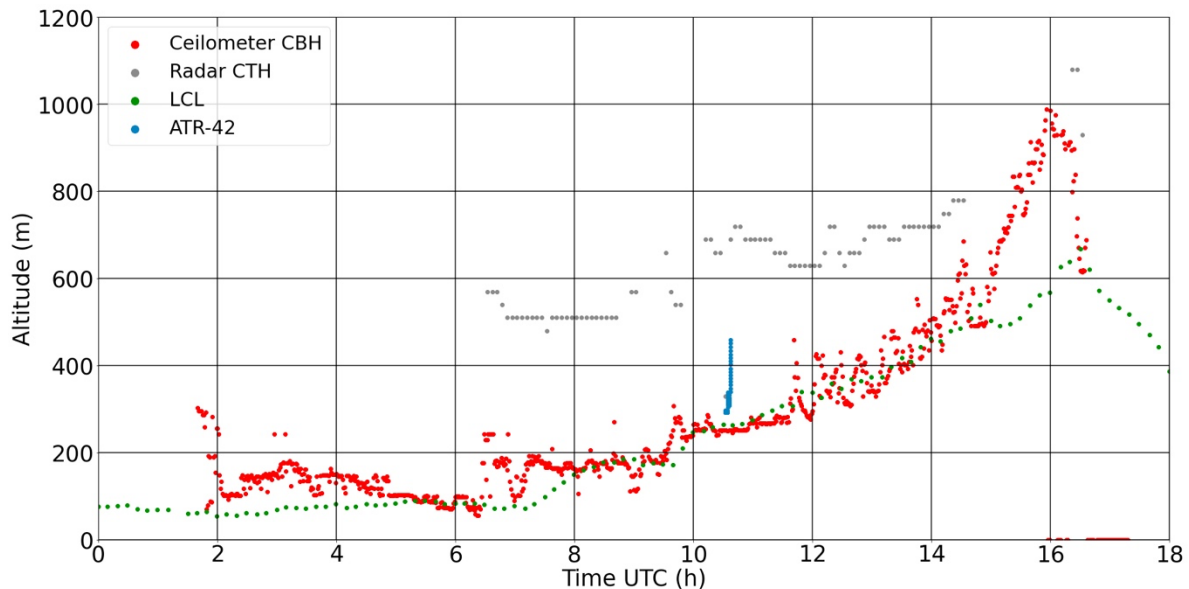


Figure 2. 3 July cloud evolution with the representation of the Cloud Base Height (CBH), the Cloud Top Height (CTH), LCL and ATR-42 flight track near Savè.

195 The diurnal cycle of LLSCs over SWA typically involves four phases: the stable phase, jet phase, stratus phase, and convective phase (Dione *et al.*, 2019; Lohou *et al.*, 2020). The stable phase begins just after sunset and is characterized by a weak monsoon flow and the cessation of buoyancy-driven turbulence within the PBL, generated by surface heating (Zouzoua *et al.*, 2021). The jet phase corresponds to the
 200 settlement of key drivers of cooler air advection. Maritime Inflow (MI), a cold and slightly humid air mass from the Guinean coast, often reaches Savè at the end of the afternoon (between 16:00 UTC and 20:00 UTC), then is followed by the NLLJ formation (Adler *et al.*, 2019). The stratus phase begins with LLSC formation when advective cooling continuously increases the relative humidity (RH) until air reaches saturation between 22:00 and 06:00 UTC. Turbulent mixing beneath the NLLJ alongside strong
 205 radiative cooling at the cloud top leads to the persistence of a thick stratus layer (Schuster *et al.*, 2013;

Babic *et al.*, 2019). The LLSCs life cycle ends during the final convective phase which begins when the PBL develops vertically due to solar heating at the surface alongside a weak radiative cooling at cloud top (*e.g.*, Ghonima *et al.*, 2016). By using dataset from Savè supersite, Zouzoua *et al.* (2021) identified three scenarios of evolution depending on the LLSCs coupling to the surface at sunrise. The coupling was assessed by the departure between the Cloud Base Height (CBH) and the Lifting Condensation Level (LCL).

The LLSCs observed on 3 July 2016 follow the four aforementioned phases and evolve by scenario C described by Zouzoua *et al.* (2021) as seen in Figure 2. The cloud is coupled to the surface at sunrise (06:30 UTC), its base rises with growing PBL until break-up occurs in the late afternoon around 16:00 UTC. The cloud deck of July 3 case stands longer (2-3 hours more) compared to other LLSCs observed during the campaign. The co-located Ka band mobile, dual-polarization Doppler radar (8.5 mm, 35.5 MHz) at Savè supersite detected light drizzle precipitation from higher clouds in a rather short period during the first hours of the convective phase, while no precipitation was detected by the surface rain gauge. Thus, this late LLSC break-up could be explained hypothetically by the evaporation of this light precipitation (Zouzoua *et al.*, 2021). Nevertheless, our focus of this study is on the diurnal cycle of LLSC as influenced by aerosols alongside planetary boundary layer dynamics rather than examining the above hypothesis, which appeared to be related to a process beyond the local scale. Therefore, our model setting is made to specifically eliminate the influence of mid-cloud layer for the purpose as described later.

On 3 July 2016, the ATR-42 flew around Savè supersite and probed the boundary layer around 10:00 UTC. The airborne instruments detected aerosol size distributions with a maximum number concentration around 3500 cm^{-3} mainly in the Aikten mode. The ATR-42 also detected an export of polluted air mass from Lomé (a coast city), which could explain the measured high aerosol concentration in the Aikten mode (Denjean *et al.*, 2020a). The measured aerosol chemical composition was mainly dominated by organics (55.3%), followed by sulfates (24.5%), ammoniac (11.2%), and nitrates (6.2%), while only a small amount of BC mass was detected around Savè (2.8%). However, the measured aerosol size distributions were found to need a correction based on aerosol refractive index to avoid bias. For this purpose, Denjean *et al.* (2020a) provided corrected profiles for various types of aerosol populations measured during the DACCIWA campaign.

2.3 Meso-NH Model

In this study, we have simulated the observed case using the Meso-NH model (Lac *et al.*, 2018). Meso-NH is a non-hydrostatic atmospheric research model that has been applied to studies in different scales ranging from synoptic to turbulent. Deployed in a limited area, the model uses advanced numerical techniques like monotonic advection schemes for scalar transport, and fourth order advection scheme for momentum (Jiang and Shu, 1996). Sub-grid turbulence is parametrized using turbulence kinetic energy (TKE) based on Deardorff turbulent mixing length. In this study, a fourth order advection scheme CEN4TH, centered on space and time, is applied with a Runge-Kutta centered 4th order temporal scheme for momentum advection (Lunet *et al.*, 2017). Aerosol and chemistry are also well represented. Here, Meso-NH version 5.4.2 is used and the relevant component modules and parametrizations for this study are described as follows.

The aerosol-cloud framework of Meso-NH version used in this study is LIMA (Liquid Ice Multiple Aerosol). LIMA includes a complete two-moment scheme predicting both the mass mixing ratio and the number concentration of aerosol species (Vié *et al.*, 2016), using a superimposition of several aerosol modes, with each mode defined by its chemical composition and size distribution. Aerosols can act as either Cloud Condensation Nuclei (CCN) or Ice Forming Nuclei (IFN). Based on the ICE3-ICE4 ice microphysics schemes (Caniaux *et al.*, 1994; Pinty and Jabouille, 1998; Lascaux *et al.*, 2006) and the two-moment warm microphysical scheme C2R2 (Cohard and Pinty, 2000), LIMA also predicts the number concentration of cloud droplets, raindrops, and pristine ice crystals. For modeling boundary layer cloud in LES mode, a pseudo-prognostic approach for supersaturation was developed (Thouaron *et al.*, 2012) to limit the droplet concentration production and to represent cloud-top supersaturation better. A variant to C2R2, called KHKO, was developed by Geoffroy *et al.* (2008) for clouds producing drizzle following Khairoutdinov and Kogan (2000) parametrization. The clouds suitable for KHKO are thin and thus low precipitating warm clouds. The precipitating hydrometeors are drizzle only and their diameter are of the order of several dozens of micrometers. These modifications for KHKO were brought inside LIMA warm phase in order to better represent drizzle.

To better represent aerosols, we have used the aerosol module ORILAM (Organic Inorganic Lognormal Aerosols Model) in this study and coupled it with Meso-NH to interconnect the cloud microphysics module with LIMA (Tulet *et al.*, 2005). ORILAM describes the size distribution and the chemical composition of aerosols using two lognormal functions respectively for the Aitken and accumulations mode. These modes are internally mixed. For each of them, the model computes the evolution of the primary species (black carbon and primary organic carbon), three inorganic ions (NO_3^- , NH_4^+ , SO_4^{2-}), and condensed water. ORILAM includes a Second Organic Aerosols (SOA) module (Tulet *et al.*, 2006) that is, however, not included in this study. Three moments (the zeroth, third, and sixth) are considered for each mode to compute the evolution of total number, median diameter, and geometric standard deviation. Note that the choice of the 6th moment is numerical since it allows one to calculate the coagulation coefficients explicitly and to facilitate the integration of the aerosol solver. The size distribution can evolve through a particle coagulation process with both intra- and intermodal calculations. It can also evolve through condensation and merging between modes. ORILAM includes the CCN activation scheme of Abdul-Razzak and Ghan (2004) in order to replace the one of LIMA to calculate the number of activated CCN. The use of ORILAM needs to activate the gas phase chemistry scheme of Meso-NH (Tulet *et al.*, 2003; Mari *et al.*, 2004) using the EXQSSA solver. ORILAM has a module for gas-particle thermodynamic equilibrium (EQSAM for inorganics and MPMPO for organics) that allows the model to calculate the contents of inorganic and organic compositions including water within the aerosol (*e.g.*, Metzger *et al.*, 2002; Griffin *et al.*, 2003). The solver will combine moment 0 (integrated number) and 3 (integrated new volume which integrates the hygroscopic growth) to calculate the new dimensional distribution (Tulet *et al.*, 2005, 2006). ORILAM directly computes the evolution of aerosol extinction, SSA, and asymmetry factors that are coupled online with the radiation scheme of Meso-NH for the 6 short wavelengths from the aerosol chemical composition and size parameters (Aouizerats *et al.*, 2010).

ECMWF radiation module is adopted in this study. Based on the two-stream method, this module calculates the atmospheric heating rate and then net surface radiative forcing. Longwave radiation scheme

used is the Rapid Radiation Transfer Model (RRTM; Mlawer *et al.*, 1997), based on the correlated k-distribution method. It integrates 16 bands and 140 g points (Morcrette, 2002). The shortwave scheme uses the photon path distribution method (Fouquart and Bonnel, 1980) in six spectral bands. Fluxes are calculated independently in clear and cloudy portions before being aggregated. The liquid cloud effective radius is computed from the liquid water content with the Martin *et al.* (1994) parametrization.

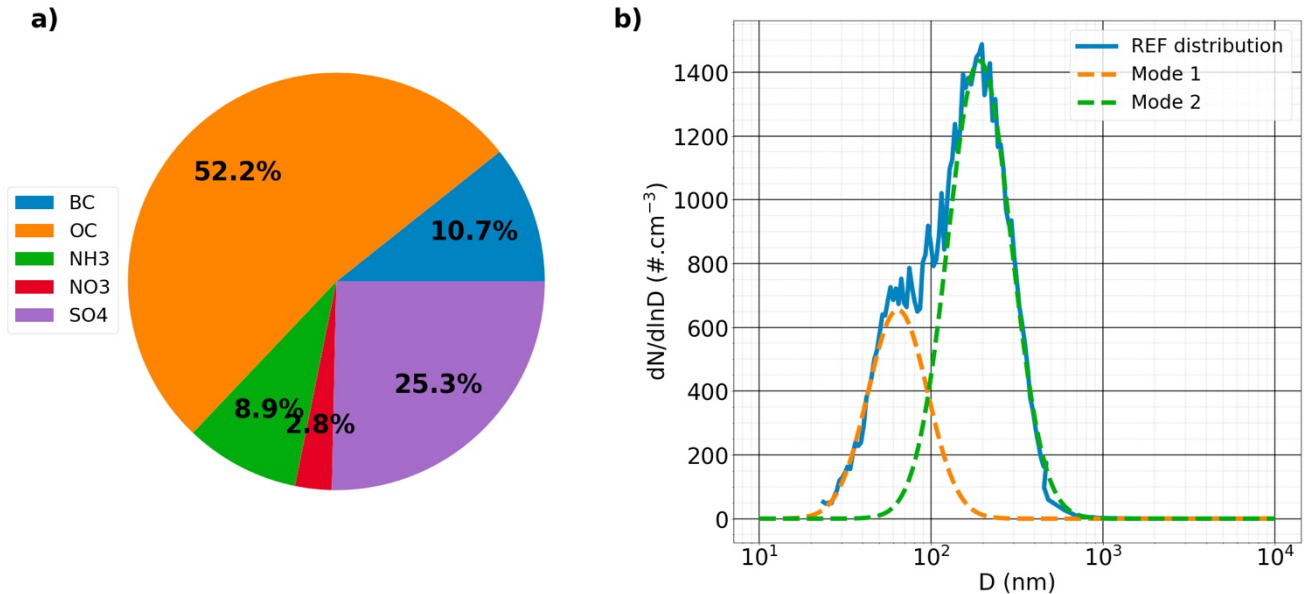
The surface model used in our modeling is the SURFEX, which is a standardized surface module containing surface schemes externalized of Meso-NH (Masson *et al.*, 2013). With SURFEX, each grid point can be split into four tiles: land, town, sea, and inland water (lake, rivers). In case of a shrubs surface, the interactions between soil, biological processes, and atmosphere are calculated by ISBA parametrization (Noilhan and Planton, 1989). Several evapotranspiration formulations are available for simulating plants and CO₂ fluxes. Soil is represented as a bucket of two or three layers. The land tile can be separated into as many as 19 subtiles following the type of vegetation.

300 2.4 Model settings

Based on the observations and the capability of the model, a reference case (REF) was first designed to simulate in LES. The reference case serves as a base to reproduce the major features of the observed LLSCs life cycle particularly using an observed aerosol profile. It also serves as a reference for further sensitivity simulations with different aerosol configurations to study the impacts of aerosol composition alongside abundance on LLSCs.

The domain is a 3D box of 9.6 km x 9.6 km x 2 km in size, with a horizontal resolution of 40 m x 40 m. Note that the radiation module still proceeds calculations above 2 km using prescribed profiles. The vertical resolution is 10 m between 0 m and 1200 m then 40 m above until 2 km of altitude to resolve explicitly the important turbulent eddies. A periodic boundary condition on the horizontal directions is applied and an absorbing layer is set between 1.8 and 2 km height. A thermodynamic perturbation is deployed to activate turbulence at the beginning of the simulation at 23:00 UTC of 2 July and the spin-up is 1h (though observed clouds formed around 02:00 UTC). A subsidence profile is applied following Bellon and Stevens (2013) scheme $w_{subs}(z) = -w_0[1 - \exp(-z/z_w)]$, with $w_0 = 15 \text{ mm s}^{-1}$ and $z_w = 250 \text{ m}$. This subsidence profile is applied during the entire simulation to keep a nearly constant cloud top height during the stratus phase and to better control the convective phase. The surface energy and water fluxes are simulated by SURFEX ISBA scheme, parametrized using data from Savè supersite, with the typical vegetation consisting of shrubs, crops, or taller trees, assuming a flat surface in the area around Savè. A time-step of 2s is used, which appears to be adequate based on testing runs to study the LLSCs nocturnal-diurnal variations particularly involving aerosol and cloud microphysics. The radiation scheme is called every 10 minutes. Note that previous studies regarding nocturnal stratus-stratocumulus suggested that a vertical resolution as fine as 5 meters near the cloud top would be necessary for reproducing the cloud top entrainment and thus cloud macrophysical structures (Stevens *et al.*, 2005). However, the nocturnal-diurnal life cycle in our case involves a dynamically evolving cloud top from 400 to 1200 m, particularly in the daytime, making it a difficult task to prescribe a highlighted zone for finer resolution. Our fast-testing results, on the other hand, did not suggest an alarming difference between the run with 10 m and 5 m vertical resolution (not shown). Therefore, the current vertical resolution and the time step are

selected to well cover all possible cloud tops during the simulation and to provide a best economic computational performance for modeling aerosol-cloud interaction with a fully coupled chemistry model.



330

Figure 3. Aerosol chemical mass compositions (a) and size distribution fitted into 2 modes described in Table 1 (b) used in REF.

335

	$N_a (cm^{-3})$	σ	D (nm)
Mode 1	654	1.49	63.98
Mode 2	1530	1.53	190.97

340

Table 1. REF aerosol size distribution described by two modes configured by three parameters (number concentration N_a , standard deviation σ and diameter D).

REF case is configured using the radiosondes of 2 July at 23:00 UTC for temperature, humidity, and horizontal wind components (U, V). The simulation is then controlled by tendency profiles of temperature, humidity, and horizontal wind applied homogeneously on the domain each hour. These tendency profiles are based on the hourly radiosondes launched on 3 July between 00:00 and 11:00 UTC. After 11:00 UTC, the next tendency profiles were designed based on the measurements of the microwave radiometer, the analysis of surface incoming solar radiative flux, and the cloud thickness and cover. Note that, despite these best possible efforts in configuring a set of observation-constrained tendency profiles to reproduce observed cloud field, it is difficult to eliminate the possibility that such profiles could reflect certain local thermodynamic effects however small they are. In practice, our main goal is to make the profiles to be able to force the modeled clouds reproduce observed quantities of major features such as cloud top, base, liquid water path (LWP), surface incoming solar radiation, among others, in the REF case. This would

350

355 serve the best purpose for us to address the major issue of this study, *i.e.*, the role of different aerosol profiles in the life cycle of modeled LLSCs.

We use a "background" distribution as the aerosol profile for REF simulation. This profile, as described in Denjean *et al.* (2020a), reflects the influence of aged BBA on clouds with minor influence of local anthropogenic sources. The aerosol number size distribution is dominated by a particle
360 accumulation mode centered at 190 nm and a smaller Aiken mode centered at 64 nm (Figure 3b). This profile exhibits a high loading of aerosols with a maximum of 1400 cm^{-3} detected in the accumulation mode. The aerosol chemical composition is dominated by organics (52.2%), followed by sulfates (25.3%), ammonium (8.9%), BC (10.7%), and nitrates (2.8%). The configuration of ORILAM has been initialized
365 using the REF aerosol chemical composition and size distribution given in Table 1 and Figure 3b by fitting the SMPS profiles into two lognormal modes using the "py-smps" package (Hagan *et al.*, 2022), with each mode having the same chemical composition.

3. Analysis of REF Results

3.1 Simulated LLSCs evolution

370 The simulation of the REF scenario reproduces the formation of the observed LLSCs deck on 3 July 2016 as shown in Figure 4. The formation of clouds leads, as described in section 2.2, to the end of the jet phase. The domain mean CBH, estimated from the modeled mixing ratio of cloud droplets follows the ceilometer's measurements during the stratus phase between 02:00 and 10:00 UTC, varies between 100 and 200 m of altitude. The simulated mean Cloud Top Height (CTH) evolves from 400 to 550 m of
375 altitude, well within the range from 500 to 580 m detected by the radar, though during the convective phase, the model result differs slightly from the observations.

The modeled mean simulated CBH and CTH are overestimated compared to ceilometer and radar values during some periods in late morning and afternoon. The difference between simulated and ceilometer detected CBH can be as large as 150 m of altitude at 11:00 UTC. While CTH is often overestimated by
380 100 m. Between 15:00 and 16:00 UTC, the simulated mean CBH approaches again the ceilometer readings (600 to 950 m) (no radar values are available to validate the simulated CTH). As mentioned in section 2.1, the ceilometer is a lidar while the values are derived from reflectivity vertical profiles with a 30 m of resolution. The differences between the model and the observation between 13:00 and 16:00 UTC
385 could come from the different representation of simulated result (a domain average) versus that of ceilometer detection (limited to only one vertical direction), the vertical resolution of observed profiles, the limitation of radar in detecting hydrometeors, and in the end, certain model weaknesses likely associated with a lack of hourly radiosondes during the afternoon period to provide sufficient observational constrain.

390

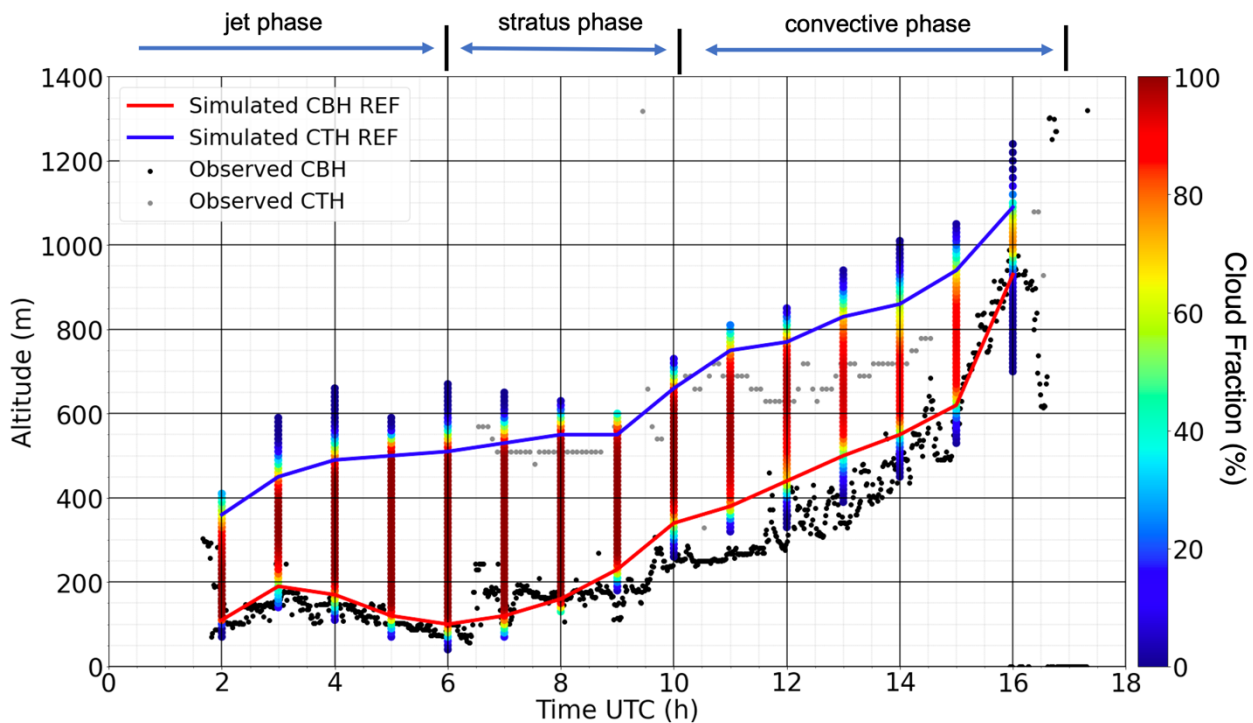


Figure 4. Simulated LLSCs deck evolution compared to Savè ceilometer and radar measurements, vertical color bars attribute cloud fraction in percentage at each altitude level. Here simulated CBH and CTH represent domain-averaged cloud base and cloud top height, respectively. Different phases might have overlaps; therefore, their marks only serve a reference purpose here.

395

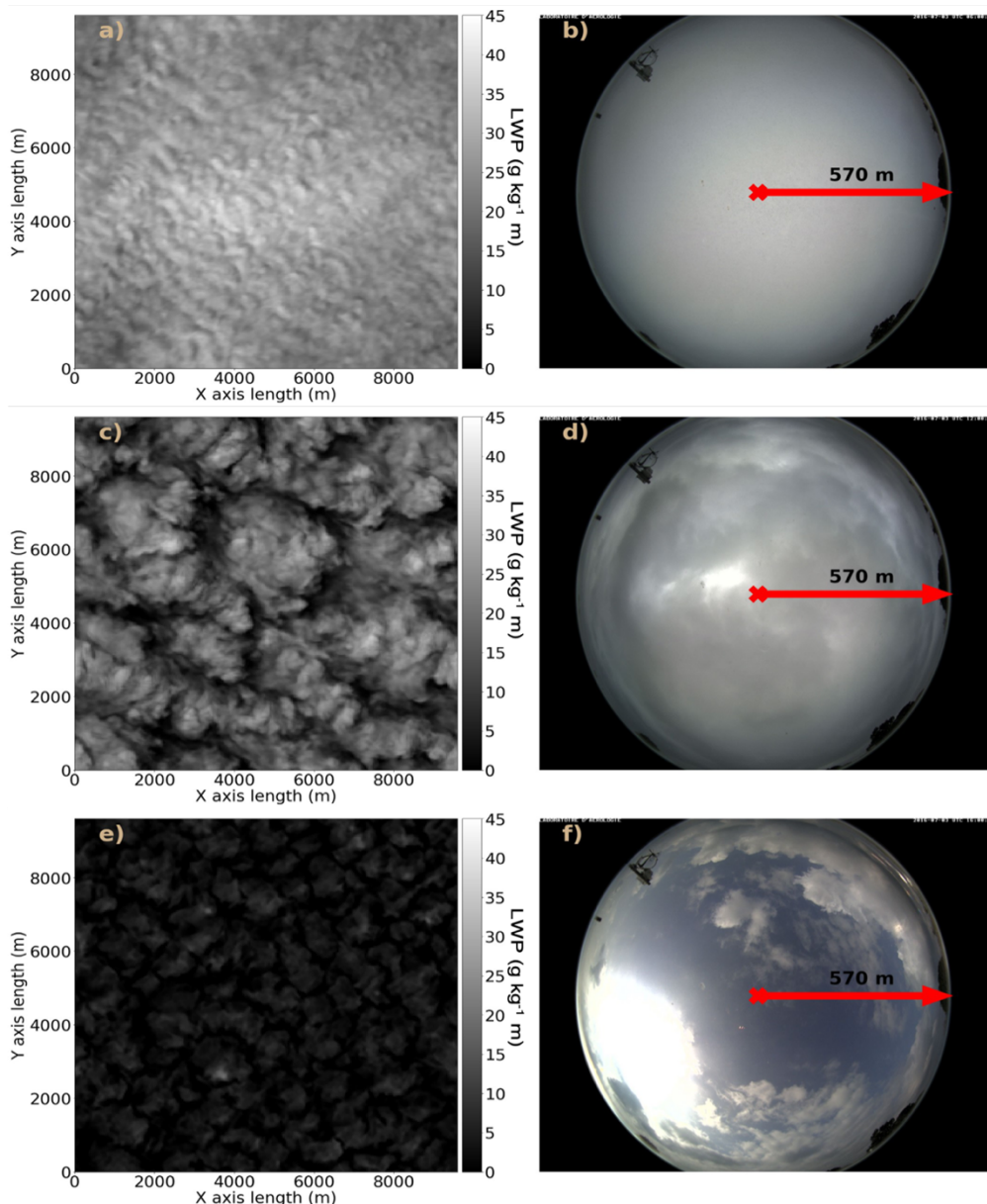
To analyze the cloud cover profile over the domain, the cloud fraction (CF) at each model layer is calculated as the percentage of all cloud pixels with a total condensed water mixing ratio exceeding 0.05 g kg^{-1} at each given model layer (Fig. 4). Note that this cloud fraction differs from the cloud fraction defined as a column metric. In addition, Liquid Water Path (LWP) at each column (Fig. 5), calculated based on cloud pixels, brings a view on the horizontal organization and homogeneity of the cloud deck. During the stratus phase, the CF is nearly equal to 100% between CBH and CTH, suggesting a homogeneous cloud deck consistent with cloud observations with sky camera (visible range) (Fig. 5, the top panels). Notably, peak LWP values between 06:00 and 12:00 UTC are quite close while domain-means differ (Fig. 5). In comparison, both peak and domain mean LWP are sharply lower at 16:00 UTC. Between 10:00 and 13:00 UTC, CF of the layers between domain mean CBH and CTH starts to decrease from near 100% to 90%, while CF at CBH and CTH decreases more substantially to reach near 60% and 80%, respectively. This leads to a less homogeneous cloud deck confirmed by the LWP map and the observation of the sky camera at 12:00 UTC shown in the middle row of Figure 5. Indeed, more cloud-free pixels begin to appear between clouds, hence sunlight is seen through the cloud deck by the cloud camera. Finally, CF continues to decrease until the end of the convection phase with a maximum barely

400

405

410

reaching 80%, and values around domain mean CBH and CTH level as low as 20% and 40%, respectively. This demonstrates the break-up of the cloud deck during convection and the cloud thinning. The bottom panels of Figure 5 show clearly the dissipation of a large number of clouds alongside substantially thinning of the others at 16:00 UTC.



420 **Figure 5.** Comparison between modeled liquid water path (LWP, $g\ kg^{-1}\ m$) and the images from Savè cloud camera at 06:00 (top), 12:00 (middle) and 16:00 UTC (bottom).

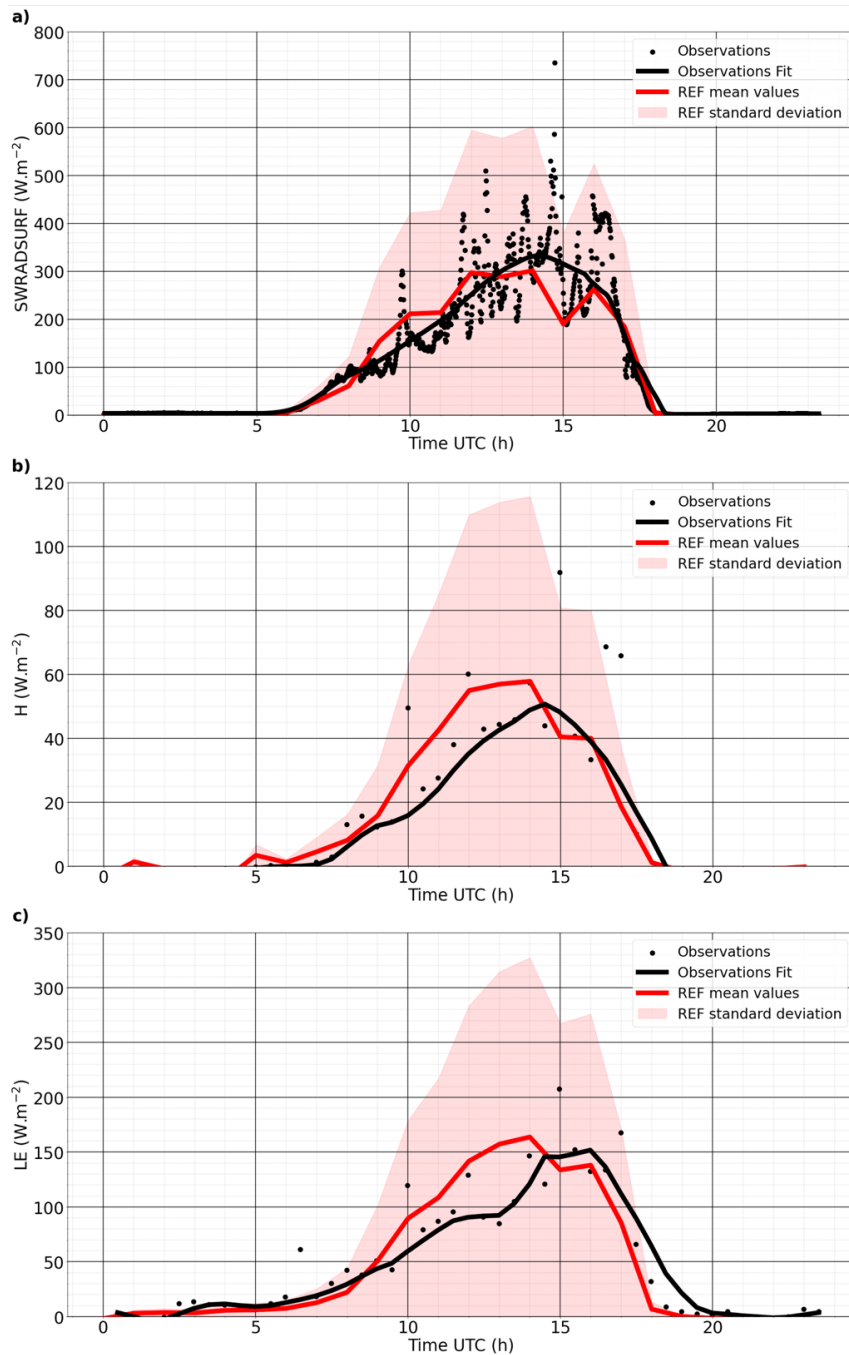


Figure 6. Comparison between Savè surface observation and REF simulation for SW radiation flux at surface (SWRADSURF, a), sensible heat flux (H, b) and latent heat flux (LE, c) all expressed in $W m^{-2}$ at the surface. The variation of REF for each parameter indicates the range of possible values these parameters can take.

Figure 6a shows the comparison between the modeled domain-average shortwave (SW) radiation flux at the surface (SWRADSURF) and the corresponding measurements performed by the energy balance station. Observed values are fitted following the LOcally Weigthed Scatterplot Smoothing (LOWESS) method (Cleveland, 1979). The temporal evolution of the modeled SWRADSURF follows the observations rather well despite some biases. After 06:00 UTC the solar radiation reaches the ground as the cloud deck thickness and covering show little variations. Thereafter, the radiative flux increases gradually by reaching near 200 W m^{-2} at the end of the stratus phase (10:00 UTC). As clouds deck becomes inhomogeneous during the convective phase (10:00 to 16:00 UTC), the modeled surface solar flux reaches a maximum of 300 W m^{-2} , which is a bit lower than the fitted 350 W m^{-2} value from measurements. When the clouds break up further, more solar radiation can reach the surface, and model and observation agree well thereafter with an exception at 15:00 UTC, where the mean modeled curve decreases to 200 W m^{-2} while the fit observed curve is near 320 W m^{-2} due to an overestimation of the cloud thickness by the model. At 16:00 UTC, both modeled and measurement values are very close around 280 W m^{-2} . Generally, the modeled maximum values are higher than the ones detected by the Savè ground instrument.

Figure 6b and 6c show that the evolutions of the modeled domain-mean latent and sensible heat flux reproduce those measured by the instrument rather well. During the night, the sensible heat flux is negative then increases to 0 W m^{-2} close to the sunrise time (06:00 UTC), indicating a reduction of the cooling close to the ground (Dione *et al.*, 2019). Between 09:00 and 14:00 UTC, the modeled sensible and latent heat flux follow the measured trends though with an overestimate of almost 70 and 18 W m^{-2} , respectively. Then the modeled curves go below the fitted observed curves at 15:00 UTC and finally both merge to almost 0 W m^{-2} after 18:00 UTC. The difference between modeled and observed heat fluxes may be again due to the different representations of area, as modeled quantities are domain-mean values while measurements are at a single point.

In Summary, the REF simulation has successfully reproduced the major observations obtained by the instruments at Savè on 3 July 2016. For example, the modeled cloud thickness and coverage reflect the measured cloud macrophysical status despite some discrepancy, likely due to a lack of hourly radiosonde data to sufficiently correct the tendency profiles to cover the entire simulation period particularly in afternoon hours. The modeled solar radiation at ground also follows the measurements very well except for certain overestimates. In addition, the sensible and latent heat fluxes measured at Savè have also been well captured by the model.

3.2 Thermodynamic, dynamical, cloud microphysical, and radiative analyses

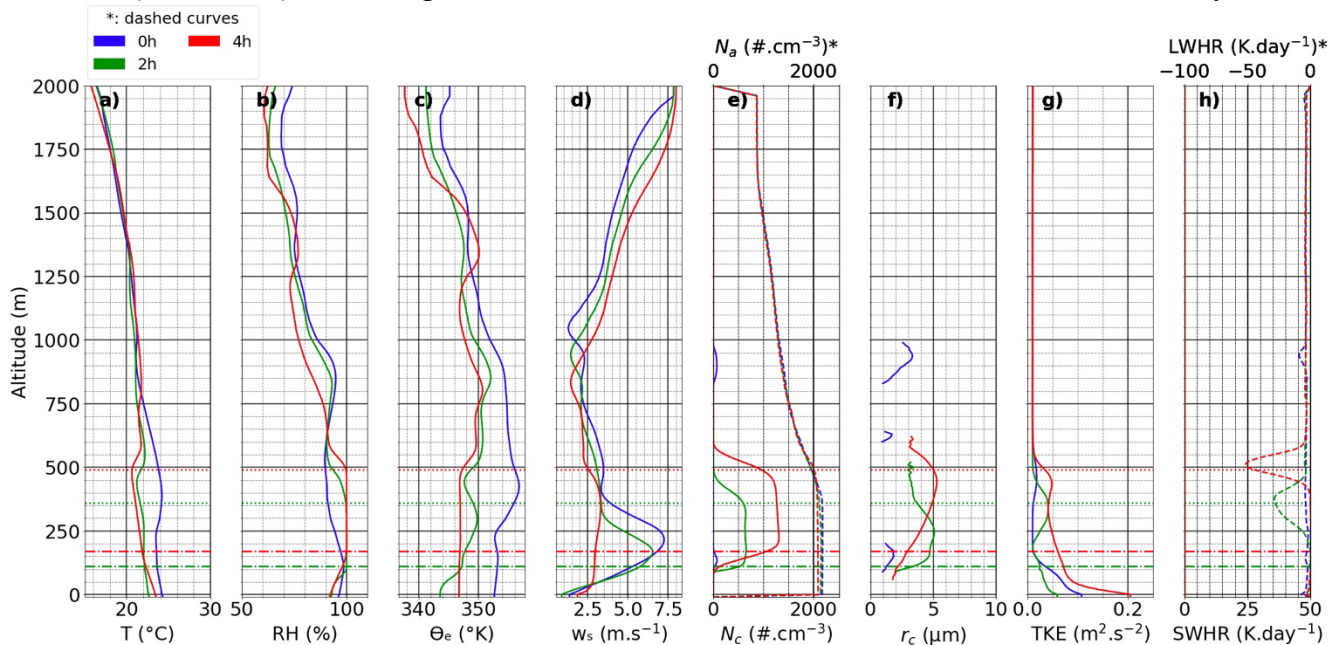
Thermodynamic, dynamical, and radiative processes and their interaction with cloud microphysics are among the key factors in determining the life cycle of LLSCs. Here we discuss the evolutions of these processes simulated by the model in the REF case to better understand the reasons behind model-observation consistency or discrepancy. The discussion will be emphasized on three periods. The first period is the transition between jet and stratus phase (between 00:00 and 04:00 UTC) to observe the formation of the clouds. The second period is the stratus phase between 06:00 and 10:00 UTC, when the stable cloud layer was observed by instruments at Savè. The third period is the convective phase between 12:00 and 17:00 UTC to study how the properties of LLSCs evolve during the break-up stage.

3.2.1 Transition jet-status phase

470 Figure 7 gives modeled domain-averaged profiles of selected macro- and microphysical features for the transition of jet to status phase, when maritime inflow already reached the site. As expected, the advection of cold and slightly humid air leads to an increase of relative humidity (RH) to reach 100% at 02:00 UTC at 100 m above ground. After this time, RH exceeds saturation between 100 and 500 m of altitude. The inversion occurs around 325 m and 500 m respectively at 02:00 UTC and at 04:00 UTC.

475 The NLLJ is well represented in modeled results as the mean wind speed (w_s) before cloud formation is greater than 7 m s^{-1} . After cloud formation, the NLLJ core nearly corresponds to the mean cloud base height (Adler *et al.*, 2019; Babic *et al.*, 2019; Lohou *et al.*, 2020). The turbulence during this period is shear-driven due to this NLLJ, yielding a well-mixed sub-cloud layer. The turbulent kinetic energy (TKE) is high above ground (0.5 to $0.2 \text{ m}^2 \text{ s}^{-2}$), then decreases to near zero above rough 200 meters at 00:00 UTC.

480 After 02:00 UTC, TKE increases at the level of CTH (350 and 500 m) and decreases at the center of clouds ($0.04 \text{ m}^2 \text{ s}^{-2}$), indicating this area is less turbulent than the extremities of the cloud layer.



485 **Figure 7.** Profiles from left to right of temperature (T, a), relative humidity (RH, b), equivalent potential temperature (θ_e , c), horizontal wind speed (w_s , d), aerosol number concentration (N_a , dashed curve, e), cloud droplets number concentration (N_c , plain curve, e), mean cloud droplet radius (r_c , f), turbulent kinetic energy (TKE, g), longwave heating rate (LWHR, dashed curve, h) and shortwave heating rate (SWHR, plain curve, h) at 00:00, 02:00 and 04:00 UTC. The horizontal dashed dot lines represent mean cloud base height (CBH) and dotted horizontal lines the mean cloud top height (CTH).

490 Cloud droplet number concentration or CDNC (N_c) is determined by the supersaturation in an updraft at cloud base and the concentration of aerosols that activate at this supersaturation. In Figure 7e, simulated aerosol concentration is the highest close to the ground then decreases with altitude up to around 2 km. This simulated aerosol profile is similar to the airborne measurements during DACCIIWA (Taylor *et al.*,

2019; Denjean *et al.*, 2020a; Deroubaix *et al.*, 2019; Flamant *et al.*, 2018). The simulated cloud microphysical features reflect a polluted condition as N_c reaches $1750 \text{ droplet cm}^{-3}$ and mean cloud droplet radius r_c around $5 \mu\text{m}$ that is not enough to form drizzle (size between 0.2 mm and 0.5 mm; Pruppacher *et al.*, 1998; Sandu *et al.*, 2008). These values are in the range of corresponding measurements at the same altitude by Taylor *et al.* (2019). The median of simulated CDNC is $500 \text{ droplets cm}^{-3}$ at the beginning of cloud formation then reaches $1750 \text{ droplets cm}^{-3}$ later, most likely due to the continuous activation of aerosol into cloud droplets.

The emission of thermal radiation by the clouds during the stratus phase creates a cooling at the cloud top as demonstrated by the evolution of modeled Long-Wave Heating Rate (LWHR) profiles at Figure 7h. The more numerous the cloud droplets are the stronger the cooling is, as shown in Fig. 7h that LWHR can reach -50 K day^{-1} . This strong longwave emission can reduce the thermal production of turbulence above the cloud top, deepening the temperature inversion. A stabilized cloud top layer by radiative cooling and a NLLJ core contributing to the shear-driven turbulence below the cloud base leads to a well-mixed cloud layer, making the LCL to correspond to the LLCSS base as seen in Figure 2 (Adler *et al.*, 2019; Lohou *et al.*, 2020).

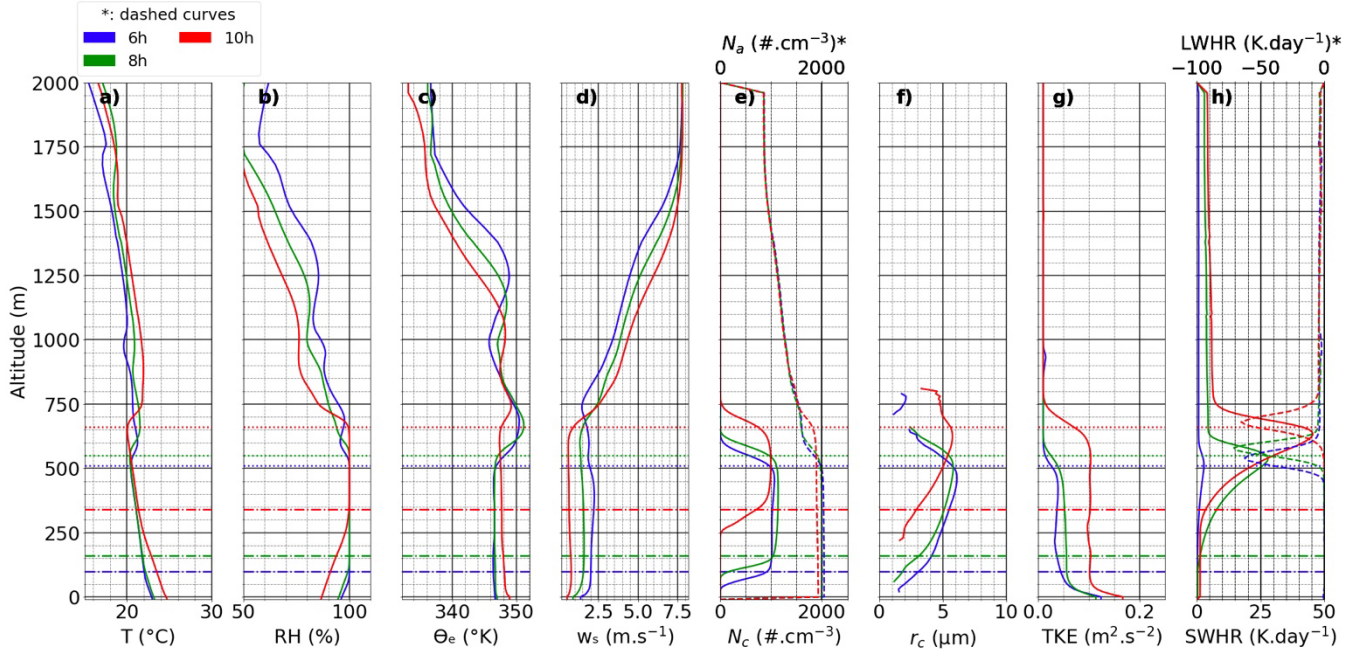
3.2.2 Stratus phase

The stratus phase starts just after the sunrise. Maintaining stratus in almost the same state throughout this phase needs certain proper temperature and humidity conditions. As shows in (Figure 8), between 06:00 and 08:00 UTC the ground temperature varies little around 23°C , supersaturation still exists between CBH and CTH, and air masses are quite well-mixed within as θ_e is near constantly at 347 K throughout the boundary layer and the inversion layer is settled where θ_e is reaching 350–351 K. The horizontal wind speed between the ground and the cloud base decreases, which indicates a weakening NLLJ core (nearly 2 m s^{-1}), then rises with altitude due to the turbulent mixing induced by the LW cooling at the cloud top during the night. The turbulence between ground and cloud center decreases to $0.03 \text{ m}^2 \text{ s}^{-2}$ then finally increases slightly to $0.04 \text{ m}^2 \text{ s}^{-2}$ at the mean CTH. The TKE is a bit stronger at 08:00 UTC, reaching $0.05 \text{ m}^2 \text{ s}^{-2}$ in the cloud layer, implying an increase of surface solar heating.

The aerosol concentration at 06:00 and 08:00 UTC is around 2000 cm^{-3} up to 500 m altitude, then decreases along altitude. This concentration is high enough to sustain a CDNC of 1100–1200 *droplets cm*⁻³ between CBH and CTH. The concentration of cloud droplets leads to a maximum layer-mean droplet radius of $6 \mu\text{m}$, which is still not enough to form drizzle. The cloud layer has an albedo close to 1 due to the high CDNC. The presence of light absorbing aerosol amplifies the Short-Wave Heating Rate (SWHR) at the cloud top by semi-direct effect. At 08:00 UTC, the SWHR and LWHR are equal to 27 K day^{-1} and -70 K day^{-1} , respectively.

At 10:00 UTC, the cloud layer starts to rise significantly, with CBH and CTH reaching 340 and 660 m, respectively. Moreover, stronger solar irradiance reaches the ground (220 W m^2), leading to the heating of the surface and the increasing of the sensible and latent heat fluxes as seen in Figure 6. It also increases the temperature near ground to 24°C and at the cloud top to 20°C . The inversion layer is observed above the cloud top between 660 and 750 m. The NLLJ core is no longer present. TKE increases to $0.1 \text{ m}^2 \text{ s}^{-2}$ throughout the vertical layer from 50 meter above the ground to a level just below the cloud top. This

enhancement of turbulence is expected to increase entrainment entering the cloud from above as well. The SWHR increases to $45 K day^{-1}$, almost compensates the LWHR cooling of $65 K day^{-1}$.



535

Figure 8. Profiles from left to right of temperature (T , a), relative humidity (RH , b), equivalent potential temperature (θ_e , c), horizontal wind speed (w_s , d), aerosol number concentration (N_a , dashed curve, e), cloud droplets number concentration (N_c , plain curve, e), cloud droplet radius (r_c , f), turbulent kinetic energy (TKE, g), longwave heating rate (LWHR, dashed curve, h) and shortwave heating rate (SWHR, plain curve, h) at 06:00, 08:00 and 10:00 UTC. Dashdot horizontal lines represent mean cloud base height (CBH) and dotted horizontal lines the mean cloud top height (CTH).

540

3.2.3 Convective phase

This phase extends from 12:00 to 17:00 UTC on 3 July 2016. During this period, surface SW radiation flux is maximized at $300 W m^{-2}$ (Figure 6), leading to an intense surface heating. As a result, the ground temperature evolves from 25 to 27 °C as seen at Figure 9. Convection of humid air masses causes the CBH and CTH to rise from 450 to 925 m and from 760 to 1100 m, respectively. The formation of clouds is still possible due to RH exceeding 100% in upper altitude. Moreover, at 16:00 UTC, the equivalent potential temperature decreases above 450 m of altitude, indicating air masses become more unstable with altitude. The horizontal wind speed is weak at the beginning of the phase with $0.5 m s^{-1}$ at ground level but increases along time to reach $1 m s^{-1}$ at ground and $3 m s^{-1}$ around 700m. This increase coincides the dissipation of the LLSCs and indicates the arrival of the marine inflow.

550

The turbulence profiles evolve along altitude during the convection phase, reaching $0.075 m^2 s^{-2}$ in center of clouds and almost zero near 850 m at 12:00 UTC. By 14:00 UTC, TKE reaches $0.25 m^2 s^{-2}$ inside the cloud, indicating a reinforcement of turbulence. At 16:00 UTC, TKE decreases near the ground but increases at cloud level to a value of $1.5 m^2 s^{-2}$, showing a strong turbulence layer there. This layer further moves to an upper altitude after 17:00 UTC.

555

The aerosol distribution varies along with the dynamical situation. The maximum aerosols concentration reaches 1800 cm^{-3} below 800 m at 12:00 and 1700 cm^{-3} below 1000 m at 17:00 UTC. As a result, the domain mean CDNC has a maximum value of $900 \text{ droplets cm}^{-3}$ at 12:00 UTC. This value decreases along time as more clouds dissipate. After clouds start to break and become thinner, reduced cloud coverage allows more solar radiation to reach the ground. The maximum value of SWHR drastically changes from 45 K day^{-1} at 12:00 UTC (almost compensating cloud top cooling) to about 10 K day^{-1} at 16:00 UTC. The cloud top LW cooling is near constant at the end of convection phase with -45 K day^{-1} .

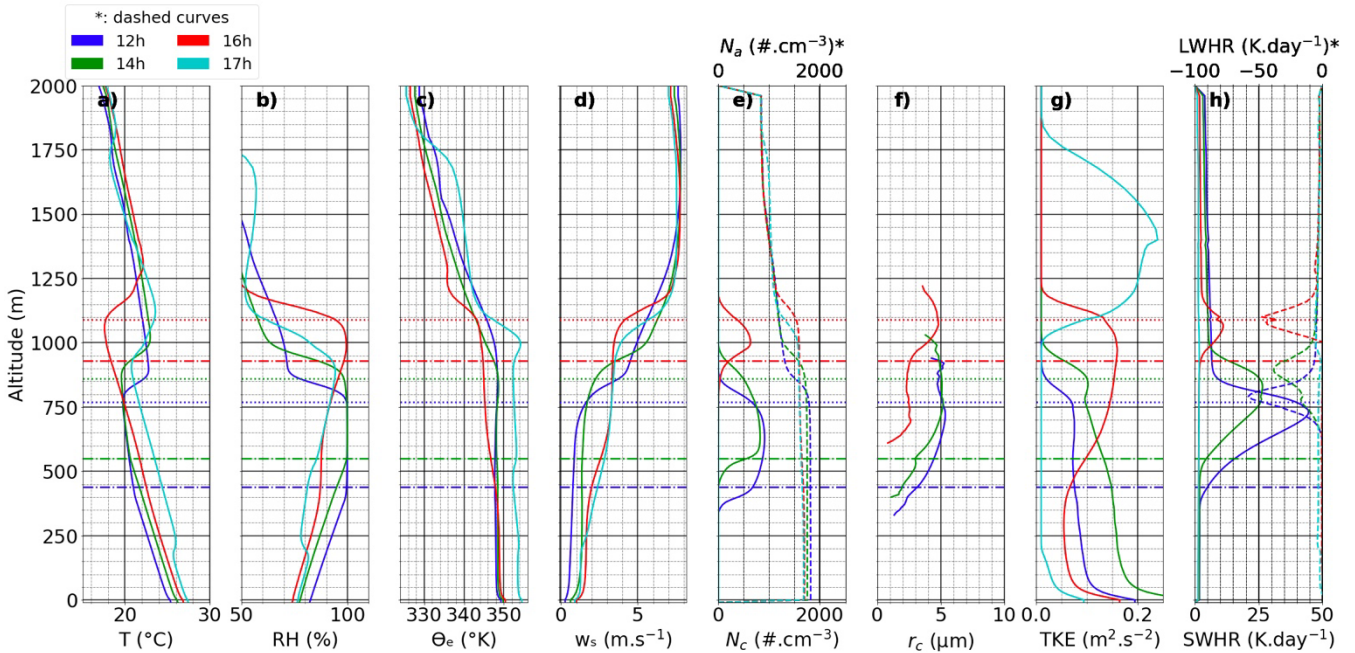


Figure 9. Profiles from left to right of temperature (T, a), relative humidity (RH, b), equivalent potential temperature (θ_e , c), horizontal wind speed (w_s , d), aerosol number concentration (N_a , dashed curve, e), cloud droplets number concentration (N_c , plain curve, e), cloud droplet radius (r_c , f), turbulent kinetic energy (TKE, g), longwave heating rate (LWHR, dashed curve, h) and shortwave heating rate (SWHR, plain curve, h) at 12:00, 14:00, 16:00 and 17:00 UTC. Dash-dot horizontal lines represent mean cloud base height (CBH) and dotted horizontal lines the mean cloud top height (CTH).

4. Sensitivity Study to Examine the Influence of Different Aerosol Profiles on LLSC Life Cycle

Previous studies have indicated that the life cycle of stratus or stratocumulus within planetary boundary layer depends on the subtle balance among several critical while interconnected forcings including surface heat fluxes, cloud top and base radiative profiles, and thus turbulent mixing (e.g., Stevens *et al.*, 2005; Dussen *et al.*, 2014, Ghonima *et al.*, 2016). Apparently, our simulation results of the REF case support previous findings particularly for cases over land with surface sensible heat playing a significant role. Nevertheless, the role of aerosols in such a life cycle have rarely been examined in depth. Given the critical role of aerosols in determining cloud macro- and microphysical features and thus radiation, this is a critical issue to address in order to advance our understanding of the LLSC life cycle. A unique component of our study is the deployment of an interactive aerosol and atmospheric chemistry

module in this observation-constrained modeling effort. In the following section we will discuss the likely impacts of aerosol variations in both number concentration and chemical composition on the life cycle of observed LLSCs.

585

4.1 Aerosol profiles used in sensitivity simulations

The result of REF simulation has demonstrated that the Meso-NH model is able to reproduce many observed features of the July 3 LLSC case despite certain biases. Moreover, the dynamical, thermodynamic, and aerosol parameters are reasonably captured by the model. To further reveal the impacts of aerosols from different emission sources on the life cycle and key aerosol-cloud-radiation processes of modeled July 3 2023 LLSC case, we have configured two additional aerosol scenarios differing from the one used in REF run, based on observations during the field campaign (Figure A1 and Table 2), then applied them in a set of sensitivity simulations that would be otherwise the same as the configuration of REF simulation. Comparing to REF case, aerosol profile of POL has a slightly higher peak number concentration but in a different mode. In addition, sulfate mass ratio in POL aerosol profile is much higher than that of REF profile, while organic carbon mass ratios are quite close in both profiles.

590
595

Case		$N_a (cm^{-3})$	σ	D (nm)
POL	Mode 1	17100	1.54	55.19
	Mode 2	2650	2.14	101.83
CLEAN	Mode 1	65	1.49	63.98
	Mode 2	153	1.53	190.97

Table 2. Aerosol size distribution parameters for POL and CLEAN, runs including number concentration, standard deviation, and diameter For two aerosol modes.

600

To investigate the impacts of anthropogenic and biomass burning sources on cloud life cycle, three additional numerical experiments were performed in addition to REF (Table 2) The first is an experiment with aerosol profile that reflects an influence of heavy anthropogenic pollution, obtained based on the aerosol chemical composition and size distribution observed by Brito *et al.* (2018) and Denjean *et al.* (2020a) within urban plumes originated from cities of Lomé, Accra and Abidjan, hereafter referred as POL. The second is an experiment designed using a clean aerosol profile derived by dividing REF aerosol concentration by 10, called CLEAN. The last one contains three experiments without aerosol semi-direct effect for CLEAN, POL, and REF aerosol profiles, respectively, called ADEOFF runs, which form paired simulations correspondingly with original CLEAN, POL, and REF runs, i.e., the ADEON runs of these scenarios.

610

4.2 Impact of aerosol loads on micro- and macrophysical properties of LLSCs

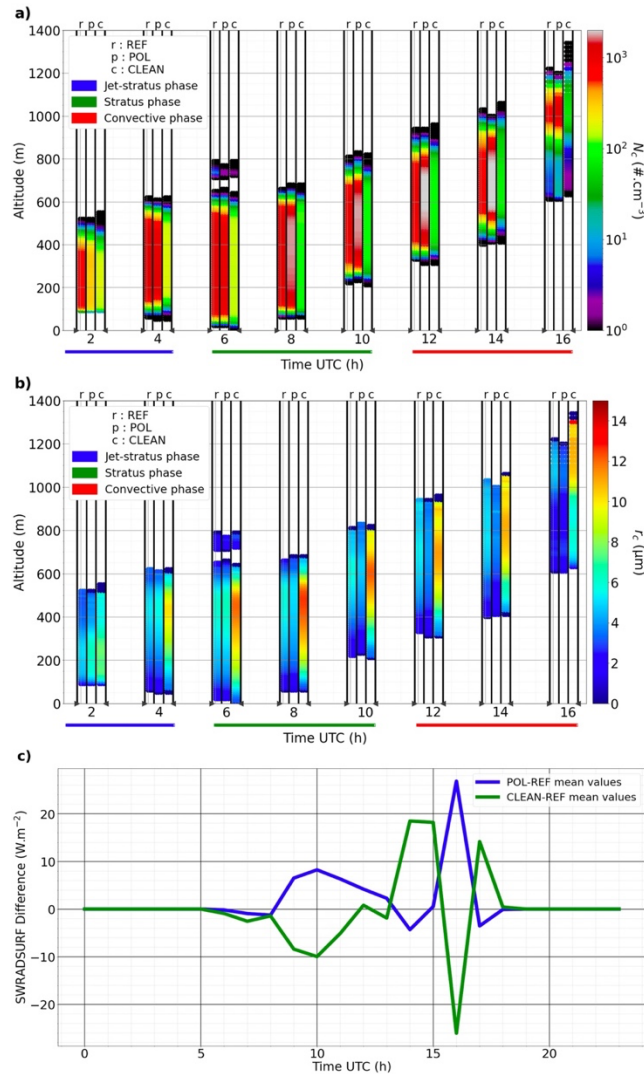
Regarding the modeled macrophysical features, the domain mean CBH and CTH and cloud fraction of REF and POL are almost the same until 08:00 UTC (Figure 4 and A2). After sunrise, the mean CBH

615 in POL is about 10 m lower than that in REF, reaching 340 m at 10:00 UTC, while the mean CTH is only
10 m higher at 940 m at 15:00 UTC, indicating a slightly thinner cloud layer in POL than REF. The cloud
fractions in both cases are also largely the same until the extensive break-up occurs, when the cloud extent
in POL displays an evident difference from that in REF, i.e., 670 m thick (from 630 to 1300 m above the
620 ground) at 16 UTC in POL versus 540 m in REF. On the other hand, POL and REF have produced clearly
different cloud microphysical features including droplet number concentrations alongside mean radius
throughout the lifetime of modeled clouds (Figure 10a and 10b). At the cloud formation (02:00 UTC),
despite having similar liquid water content (LWC) around 0.35 g m^{-3} at 250 m in both cases, N_c^{POL} reaches
 $333 \text{ droplets cm}^{-3}$ and r_c^{POL} $6.45 \text{ }\mu\text{m}$ instead of $653 \text{ droplets cm}^{-3}$ and $5.1 \text{ }\mu\text{m}$ for REF case, indicating a
625 result of differences mainly in Mode 2 aerosol numbers between the two scenarios (at 02:00 UTC the
updraft near cloud base is rather weak at less than 0.30 m s^{-1} in both cases). This trend is reversed at 06:00
UTC when the CDNC and radius are equal to $1208 \text{ droplets cm}^{-3}$ and $6.43 \text{ }\mu\text{m}$ in POL, and 1305 droplets
 cm^{-3} and $6.12 \text{ }\mu\text{m}$ in REF, respectively. After 08 UTC and until the cloud break up, N_c^{POL} is superior to
 N_c^{REF} by reaching a maximum difference of $1425 \text{ droplets cm}^{-3}$ at 14:00 UTC. Their respective radii are
 $4.42 \text{ }\mu\text{m}$ and $5.18 \text{ }\mu\text{m}$ while the liquid water content profiles are quite the same as near 0.47 g m^{-3} at 750
630 m. The difference between POL and REF in CDNC after sunrise suggests that the activation favors the
POL profile with higher sulfate content when updraft is strengthened. These results are in good agreement
with the ACPIM parcel model simulation done by Taylor *et al.* (2019) where CDNC varies in a range of
 $500\text{--}1400 \text{ droplets cm}^{-3}$ depending on the inland or offshore (offshore + local emissions) aerosols origin.

The difference between CLEAN and REF in cloud macrophysical features such as CBH and CTH is
635 visible though largely limited to a few tens of meters. However, their differences in cloud fraction and
microphysical features are rather significant. As expected, from formation to break-up of the clouds,
 N_c^{CLEAN} is lower than N_c^{REF} and r_c^{CLEAN} is larger than r_c^{REF} . At 02:00 UTC, N_c^{CLEAN} has a maximum value
of $181 \text{ droplets cm}^{-3}$ and r_c^{CLEAN} of $7.58 \text{ }\mu\text{m}$, in comparison to $653 \text{ droplets cm}^{-3}$ and $5.1 \text{ }\mu\text{m}$ for N_c^{REF} and
 r_c^{REF} respectively with the same liquid water content value (0.35 g m^{-3}). r_c^{CLEAN} further increases to 12.55
640 μm at 08:00 UTC, then decreases slowly to a maximum value of $10.97 \text{ }\mu\text{m}$ at 14:00 UTC with LWC^{CLEAN}
reaches near 0.45 g m^{-3} instead of 0.49 g m^{-3} for LWC^{REF} , likely due to an increased activation ratio of
aerosols after sunrise. Despite a relatively larger droplet size in CLEAN than POL and REF case, there is
no clear sign of massive formation of drizzles even during the convection stage (Fig. 10). Nevertheless,
sedimentation thus evaporation of larger droplets from entrainment zone and cloud base could likely
645 create a thermodynamic perturbation (e.g., Stevens *et al.*, 1998; Jiang *et al.*, 2002). In a LES simulations
using passive aerosol profile for July 4-5 DACCIIWA case, Dearden *et al.* (2018) found that the
sedimentation would remove droplets from the entrainment zone thus, through a feedback, lead to a cloud
deck with higher LWP while smaller CF than the case where sedimentation is completely excluded. This
could imply a similar contrast between CLEAN and the two polluted cases in our simulations, by simply
650 assuming the total sedimentation amount is proportional to the droplet size (i.e., inversely to the CDNC),
though the quantity of such a perturbation seems rather small here, not to mention the more sophisticated
feedback involved in our case introduced by the dynamic aerosol-cloud interaction in our model.

As demonstrated from above discussions that modeled cloud microphysical features respond to the
variation of aerosol number concentration as expected, i.e., higher aerosol concentration leads to higher
655 cloud droplet number concentration (POL > REF > CLEAN) while smaller mean droplet radius (POL <

660 REF < CLEAN) and hence a higher cloud reflectivity (POL > REF > CLEAN). Though exception does exist. For example, differences in the aerosol size distribution and chemical composition between REF and POL could lead to an outcome opposite to the general expectation particularly under a weak dynamical condition. As shown in Fig. 10c, the response of the incoming solar radiation at ground (SWRADSURF) does not always follow such an expectation in cloud microphysics and thus reflectivity in responding to aerosol variation. In fact, SWRADSURF appears to be higher in POL than REF from sunrise to 13:00 UTC, and the values in both runs are also clearly higher than that in CLEAN. This tendency is only reversed after 13:00 UTC when solar flux reaches its peak until the break-up stage.



665 **Figure 10.** Evolution of cloud droplets concentration N_c (top) and cloud droplets radius r_c (middle) with the scenarios given and designated by letter a (REF), b (POL) and c (CLEAN). Bottom panel gives the evolution of mean domain SWRADSURF differences between POL / CLEAN and REF.

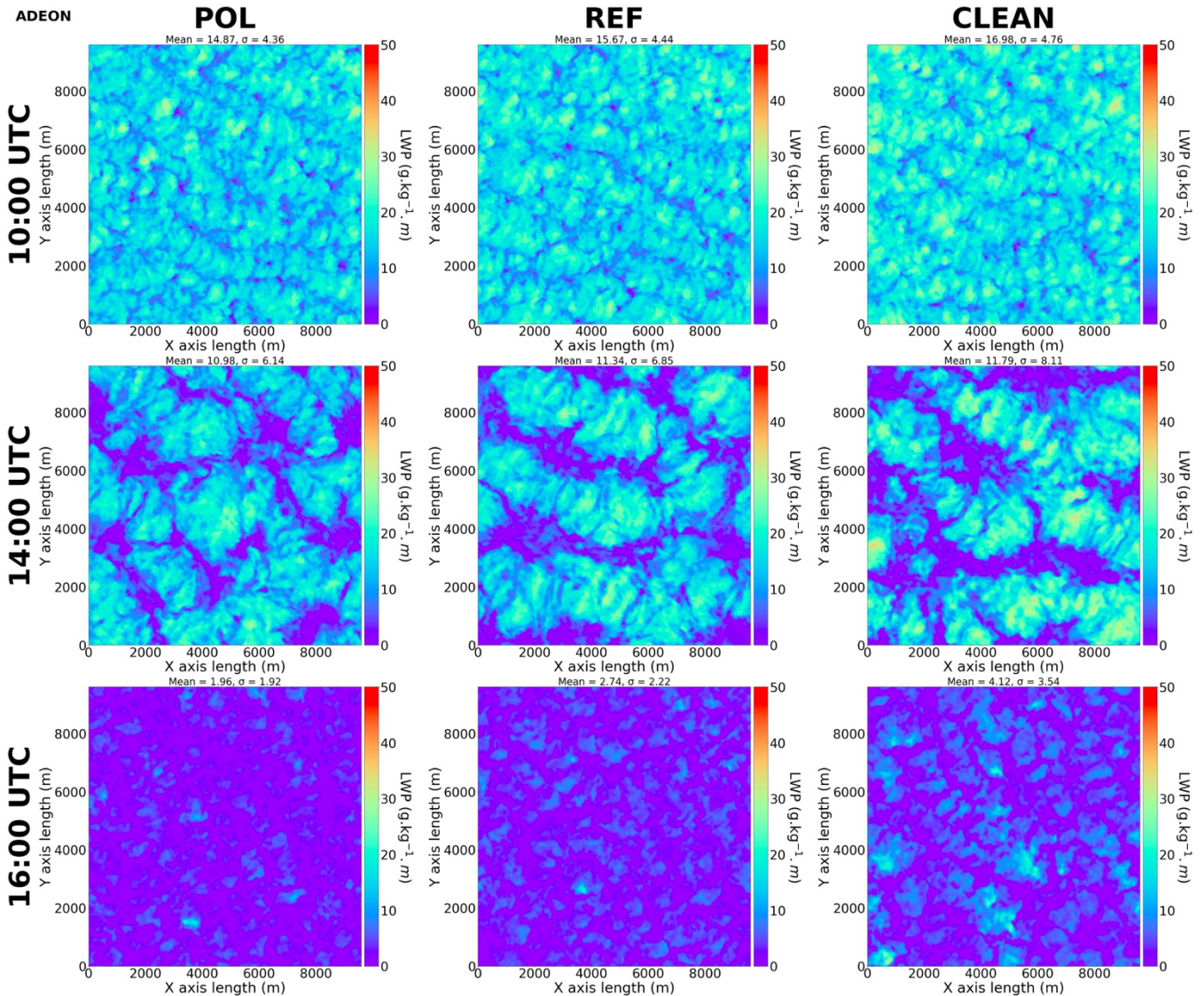


Figure 11. Liquid water path (LWP, $g\ kg^{-1}\ m$) in POL (left column), REF (mid-column), and CLEAN (right column) runs at 10:00 UTC (top row), 14:00 UTC (middle row), and 16:00 UTC (bottom row).

Figure 11 shows that the major reason behind the above-described trend of SWRADSURF is the difference in cloud fraction in competing with the effect brought by different cloud reflectivity of various runs, especially before noon when zenith angle is still high. After sunrise, the cloud top starts to rise and cloud layer becomes thicker. In the meantime, this upward development brings a downward entrainment of dry air from the temperature inversion zone above the cloud top and causes evaporation in the cloud.

For a cloud with a large quantity of very small droplets as in POL and REF, the evaporation rate of

droplets would exceed that in CLEAN case, thus more cloud-void spaces or a thinner cloud layer would form much easier than in the latter case. Note that a similar macrophysical response to aerosol concentration variation (in a simple high versus low setting) was also suggested in a marine cloud case though with a coarse vertical resolution of 50 m (Wang *et al.*, 2003). As shown in Fig. 11 and Table 3, cloud layer in CLEAN is slightly denser than those in POL and REF while cloud-void or thin cloud pixels account for a substantially lower ratio within the domain. Thus, before noontime, cloud reflectivity seems to become the secondary factor comparing to cloud fraction in determining the value of SWRADSURF. As a result, SWRADSURF in CLEAN is significantly lower than REF then POL until zenith angle becomes lower closer to noontime. The lower SWRADSURF in CLEAN would also have reduced the turbulent mixing as well as delayed the convection that would cause extensive cloud break-up. At 14:00 UTC, difference in cloud thickness and cloud-void space still exists but becomes relatively smaller among the three different runs (Fig. 11 and Table 3), cloud reflectivity now becomes the primary reason to cause a different SWRADSURF as shown in Fig. 10 (bottom panel). Interestingly, modeled clouds in POL and REF appear to dissipate earlier and much faster than in CLEAN in the break-up stage (Fig. 11, bottom panel).

	LWP 10 UTC	PCP 10 UTC	LWP 14 UTC	PCP 14 UTC	LWP 16 UTC	PCP 16 UTC
POL	14.87	12.79	10.98	42.17	1.96	99.66
REF	15.67	10.11	11.34	42.69	2.74	99.67
CLEAN	16.98	6.95	11.79	44.93	4.12	94.47

Table 3. Domain averaged liquid water path (LWP; $g\ kg^{-1}\ m$) and poor-cloud pixel percentage (PCP, defined by the percentage of pixels where $LWP < 10\ g\ kg^{-1}\ m$; percentage) in three different runs.

Looking into various timely varying metrics of LWP in different model runs, we find that in general, LWP is inversely promotional to CDNC, as $LWP\ in\ POL < LWP\ in\ REF < LWP\ in\ CLEAN$, and this is applied to different metrics of LWP (Fig. 12, Table 3). However, in comparison, the peak LWP varies less significantly in CLEAN case, while peak LWPs in two other runs decrease with domain averaged quantities in convection stage. There were different opinions regarding the mechanisms behind such an inverse relation between LWP and CDNC (*e.g.*, Ackerman *et al.*, 2004; Bretherton *et al.*, 2007), not to mention that most such hypotheses were proposed based on the cases of marine low clouds that might not be directly applied to the cases over land. In our analysis, the difference in turbulent mixing driven by the surface radiative heating, as influenced by different microphysical features in various cases, seems having played a critical role. The situation of cloud fraction (CF) is somewhat more complicated. As shown in Table 3 and Fig. A4, CF relation with CDNC varies in different stages. An inverse relation between CF and CDNC generally stands in the earlier and later period of the convection stage, in the middle of the convection stage (13:00-15:00 UTC), the above relation, however, would reverse, alongside the vertical cloud extent as discussed previously.

As demonstrated from above discussions that modeled cloud microphysical features respond to the variation of aerosol number concentration as expected, *i.e.*, higher aerosol concentration leads to higher

cloud droplet number concentration ($POL > REF > CLEAN$) while smaller mean droplet radius ($POL < REF < CLEAN$) and hence a higher cloud reflectivity ($POL > REF > CLEAN$). Though exception does exist. For example, differences in the aerosol size distribution and chemical composition between REF and POL could lead to an outcome opposite to the general expectation particularly under a weak dynamical condition. As shown in Fig. 10c, the response of the incoming solar radiation at ground (SWRADSURF) does not always follow such an expectation in cloud microphysics and thus reflectivity in responding to aerosol variation. In fact, SWRADSURF appears to be higher in POL than REF from sunrise to 13:00 UTC, and the values in both runs are also clearly higher than that in CLEAN. This tendency is only reversed after 13:00 UTC when solar flux reaches its peak until the break-up stage.

725

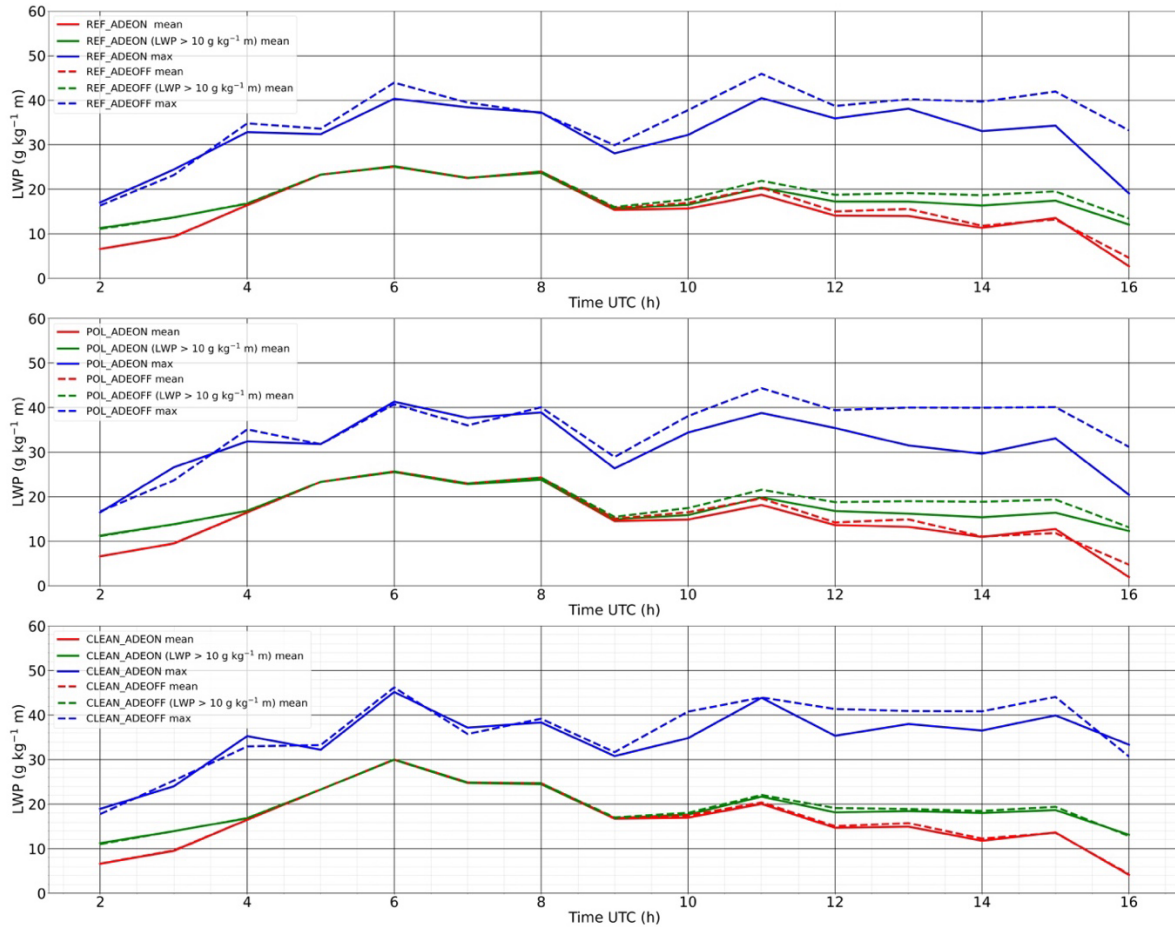


Figure 12. Domain averaged LWP (LWP mean), maximum LWP (LWP max), and domain averaged LWP over pixels where $LWP > 10 \text{ g kg}^{-1} \text{ m}$ in AODON and AODOFF runs in REF (upper panel), POL (middle panel), and CLEAN (lower panel) cases, derived using hourly model outputs.

730

4.3 Impact of aerosol semi-direct effect on LLSCs

735 The semi-direct effect of aerosols resulted from SW radiation absorption by absorbing aerosol, could affect atmospheric dynamics surrounding LLSCs and thus their life cycle. This effect has been examined in our study by comparing the results of three additional experiments, constructed accordingly in the same way as their original experiments (hereafter ADEON of REF, POL, and CLEAN) but excluding aerosol direct effects (named ADEOFF), with those of the three paired original runs. Apparently, BC is the major species behind the semi-direct effect in our case.

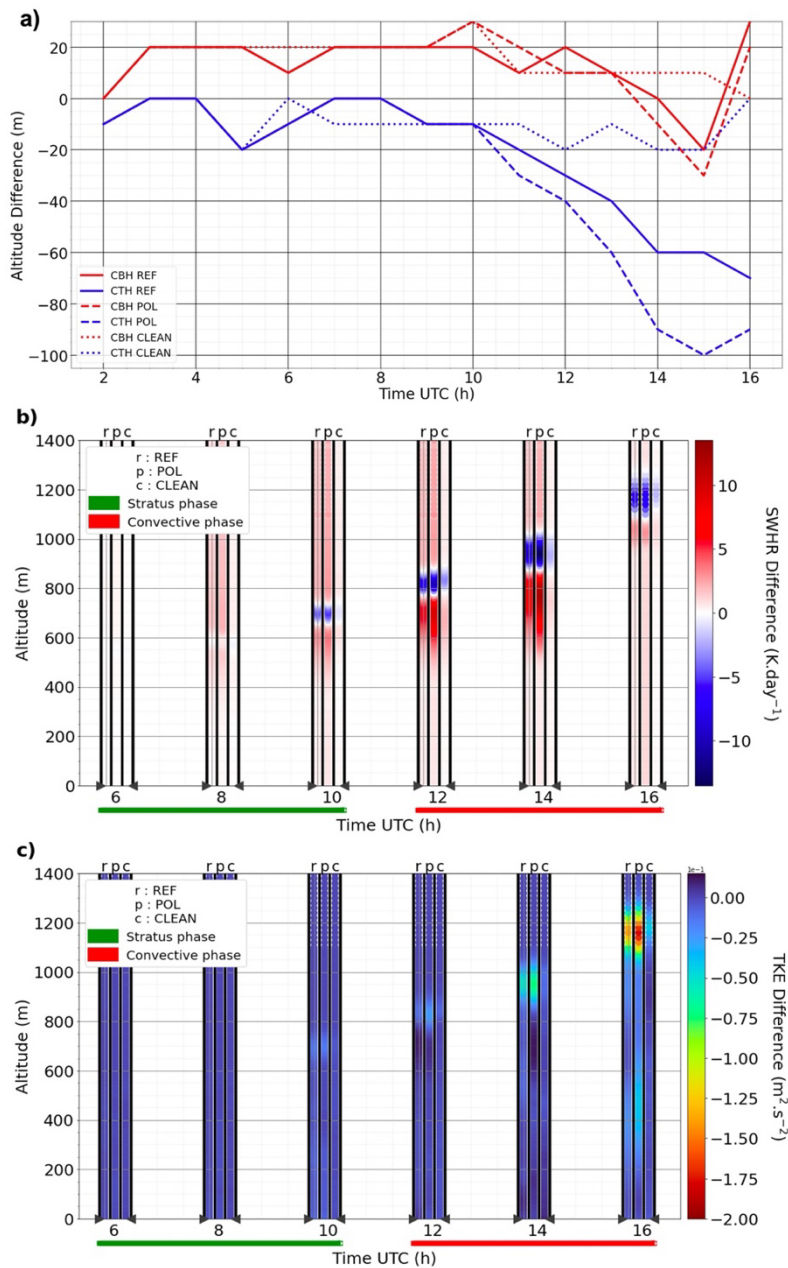
740 The changes in cloud top and base, SWHR, and TKE due to aerosol absorption and associated feedbacks are shown in Figure 13. The results demonstrate that light-absorbing BC aerosols can cause a substantial atmospheric heating accompanied by a warming tendency near the top of LLSCs (Figure 13b). At 14:00 UTC, the domain averaged heating due to BC aerosols (difference in SWHR between AODON and AODOFF) and a consequent cooling just above the cloud due mostly to the cloud top change are 12.16 K day⁻¹ and -13.14 K day⁻¹ in POL, and 7.71 K day⁻¹ and -9.24 K day⁻¹ in REF, respectively. In 745 comparison, the atmospheric heating and associated cooling of 1.30 K day⁻¹ and -2.25 K day⁻¹ in CLEAN case are clearly insignificant. Accordingly, in ADEON runs, more water vapor tends to condense onto cloud droplets under the higher relative humidity in the lower PBL and decreasing turbulent mixing (Figure 13c, with a maximum decreasing of -0.18 m² s⁻² for POL), leading to a decrease of the cloud top height, limiting entrainment, and also reducing incoming solar radiation at surface due to BC in-cloud 750 absorption. The cloud top height reduction due to the semi-direct effect in two polluted cases POL and REF is quite substantial as shown in Figure 13a, where CTH in POL and REF has decreased by up to 100 and 70 meters due to the presence of BC, respectively. On the other hand, CBH is also increased about 20 meters in both cases before break-up, suggesting a thinner cloud layer owing to the semi-direct effect. In comparison, CTH, CBH, and thus cloud vertical extent appears to be less affected in CLEAN 755 run due to its low BC content. Before break-up, in-cloud TKE below the heating layer has been reduced in some extent (Fig.13c). On the other hand, due to a lower cloud top in the polluted cases, planetary boundary layer height would also be lowered. The effect of BC absorption in lowering modeled cloud top and thinning cloud layer in POL and REF (implying a reduced upward development) is likely another factor to slow down their break-up as discussed before.

760 The impact of the semi-direct effect on other critical macrophysical features such as cloud fraction and LWP can be also seen from the model results. For instance, LWP particularly the maximum LWP is clearly lower in the AODON runs of the two polluted cases (REF and POL) (Fig. 12). In addition, an increase of cloud fraction due to the semi-direct effect can be seen throughout the convection stage until 15:00 UTC when massive cloud break-up occurs (Fig. A4). All these imply a critical role of the semi- 765 direct effect on cloud radiation.

We find that the semi-direct effect can both enhance and weaken the (negative) indirect radiative forcing as also indicated by some previous works (Lohmann and Feichter, 2001; Koch and Del Genio, 2010a; Huang *et al.*, 2014; Yamaguchi *et al.*, 2015; Stjern *et al.*, 2017; Kreidenweis *et al.*, 2019). In the convection stage before 15:00 UTC, the difference in SWRADSURF between ADEON and ADEOFF is 770 negative, reaching -33 W m⁻² and -75 W m⁻² for REF and POL at 14:00 UTC, respectively (Fig. 14c). This can be explained by an increase in cloud fraction in ADEON runs (Fig. A4, Table 3) that allows less solar irradiance to attain the surface despite the cloud layer being thinner, not to mention that solar

irradiance itself has already been reduced due to BC absorption (Fig. 12, 14c and A3). Note that the different chemical compositions between POL and REF also lead to a quantitatively different effect. Hence, the semi-direct effect contributes positively to the enhancement of (negative) indirect radiative forcing in this case. On the other hand, at 16:00 UTC, the flux difference between ADEON and ADEOFF becomes positive with values for REF and POL as 32 W m^{-2} and 66 W m^{-2} , respectively. As the clouds break up more slowly in ADEOFF during this stage due to thicker cloud layers (Fig. A3 and A4), more clouds inside the domain with increased thickness causes weaker SW irradiance reaching the ground. In other words, the semi-direct effect makes the cloud dissipate faster in the convective stage. In this case, the semi-direct effect weakens the semidirect radiative forcing.

The above results have demonstrated the important role of solar absorption by aerosols in determining the life cycle of LLSCs. The atmospheric heating by light absorbing BC would limit the elevation of cloud top, especially during the break-up stage (Koch and Del Genio, 2010b; Zhang and Zuidema, 2019). Such a heating can also increase cloud fraction then delay break-up until late afternoon, especially for clouds with higher cloud droplet number concentration in polluted environment such as in POL and REF runs (opposite to the outcome by considering aerosol number concentration only), and thus affect the indirect effect of aerosols. Note that our modeling configurations are based on the aerosol profiles that are relatively well-mixed throughout the PBL then with concentration gradually decreasing along altitude above PBL. Certain previous sensitivity experiments suggested that the location of BC layer within or above PBL could have different impacts on the development of convection, entrainment, and thus life cycle of the low clouds within PBL. For instance, Johnson *et al.* (2004) suggested that without considering the indirect effect of aerosols, BC existing within boundary layer would lower LWP by nearly 20% in a marine low stratocumulus case, where the cloud response is less sensitive to the surface shortwave heating change comparing to the situation in our case. Feingold *et al.* (2005) found that smoke plumes containing BC near the surface would reduce the cloudiness through both the atmospheric heating and weakening effect on surface heat fluxes by BC. These results though obtained with somewhat different model configurations than ours (e.g., coarser vertical resolution, different surface, etc.) are in a qualitative agreement with our findings. Nevertheless, the unique configuration of our model allows us to quantitatively examine the semi-direct effect with varying aerosol chemical compositions and thus extent of aerosol absorption. This has led us to reveal further insights of the complicated interplays among various aerosol effects besides their individual impacts on the life cycle of LLSCs.



805

Figure 13. Evolution of the difference of the mean CBH and CTH (a), SWHR (b) and TKE (c) between the simulation runs with and without aerosol direct effect (ADEON-ADEOFF) for REF, POL and CLEAN.

810

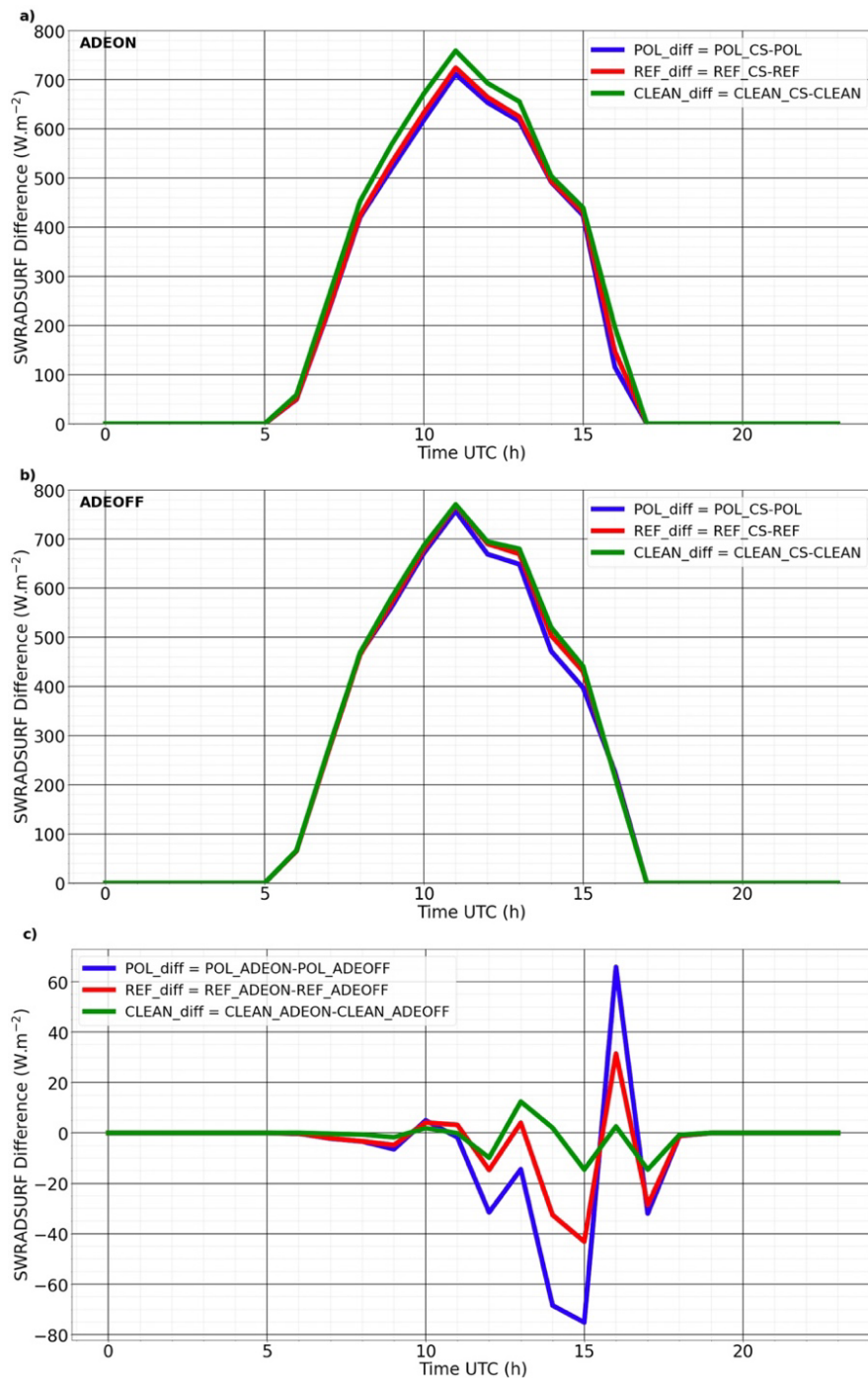


Figure 14. Mean difference surface SW radiative flux (SWRADSURF) between Clear-Sky (CS) and cloudy scenarios giving the flux dissipated by clouds in ADEON (a) and ADEOFF (b) configurations. SWRADSURF difference between ADEON and ADEOFF configuration for the three scenarios (c).

5. Conclusions

A characteristic case of the LLSCs over southern West Africa has been simulated with Meso-NH model in a Large-Eddy Simulation configuration constrained by the measurements from the DACCIWA field campaign. The model has successfully reproduced the observed nocturnal-to-diurnal life cycle alongside key macro- and microphysical features as well as surface radiative and heat fluxes. To determine the impact of aerosols on the modeled life cycle of LLSCs, sensitivity simulations using several different aerosol profiles have also been conducted. These aerosol profiles contain different size distributions and chemical compositions, reflecting the situations associated with various aerosol populations encountered during the field campaign.

The results from various sensitivity simulations suggest that both aerosol size distribution and chemical composition can effectively influence the LLSCs life cycle. The impact of the aerosol size distribution, as reflected from a comparison among simulations using aerosol profiles with different number concentrations and modal distributions, is initiated from resultant cloud microphysical features in particular the cloud droplet number concentration and mean droplet size. Such a difference created by different aerosol size distributions also affect cloud reflectivity as expected. Interestingly, we have found that the difference in cloud reflectivity caused by different aerosol concentration does not always dominate the surface incoming solar radiation and thus cloud development after sunrise. This is due to a competing factor: the cloud fraction caused by the air entrained from the inversion layer above cloud top and associated evaporation of cloud droplets as a function of CDNC, which specifically dominates the variation of surface incoming solar radiation before noontime. Clouds influenced by higher aerosol concentrations and thus having higher number concentration and smaller sizes of cloud droplets are found to evaporate more easily and thus impose a lower cloud fraction. For the same reason, clouds with higher droplet concentration are likely to break up earlier.

In addition, our sensitivity runs including versus excluding aerosol direct radiative effects have also demonstrated the impact specifically of solar absorption by black carbon on the cloud life cycle. The excessive atmospheric heating reaching $12 K day^{-1}$ introduced by black carbon in our modeled cases is found to be able to lower the cloud top height as well as liquid water path, reduce dry entrainment, and increase cloud fraction. Working with the cloud fraction response to aerosol size distribution, this heating and its consequences might delay break-up of the LLSCs until late afternoon. While beyond that point, the modeled clouds in polluted cases with higher aerosol concentrations and BC included would break up faster due to their thinner cloud layers. Therefore, the semi-direct effect can contribute positively to the indirect radiative forcing (negative in quantity) by increasing cloud fraction, or negatively by causing thinner cloud layer and thus a faster cloud break-up in late afternoon, all depending on the phase in stratiform cloud life cycle as demonstrated in this study and several previous ones.

Our study has demonstrated that the life cycle and thus the radiative forcing of LLSCs over land area of SWA can be substantially influenced by aerosols from both long-range transported biomass burning plumes and from local anthropogenic emissions. In fact, more aerosol profiles had been collected during the DACCIWA campaign besides the ones used in this study. Future research works could reveal the aerosol impact under an even broader range of aerosol properties and to examine the temporal variations of LLSCs radiative effects evolving with different large-scale meteorological

conditions with different associated airmass. More analysis on different cloud cases in SWA would also be able to assess or refute current results on semi-direct effect.

860

Code and data availability. The data obtained during the DACCIWA campaign at the Savè supersite alongside all other data used in this study are publicly available on the SEDOO database (<http://baobab.sedoo.fr/DACCIWA/>). The Meso-NH code is maintained and updated by LAERO and CNRM, it is freely available for download at <http://mesonh.aero.obs-mip.fr/mesonh52/>.

865

Author contributions. LD and CW designed the simulations and LD conducted model simulations and data analyses. LD and CW wrote this paper with contribution from all co-authors. CW advised and helped to better understand the different aspects of this research work. PT advised and trained LD for Meso-NH and ORILAM module use. CD processed and provided the aerosol profiles used in previous simulations and NM was part of this work. MZ helped to select the study case and advised during the study case construction and analysis. AD brought a critical eye to this work.

870

Competing interests. The authors declare that they have no conflict of interest.

875

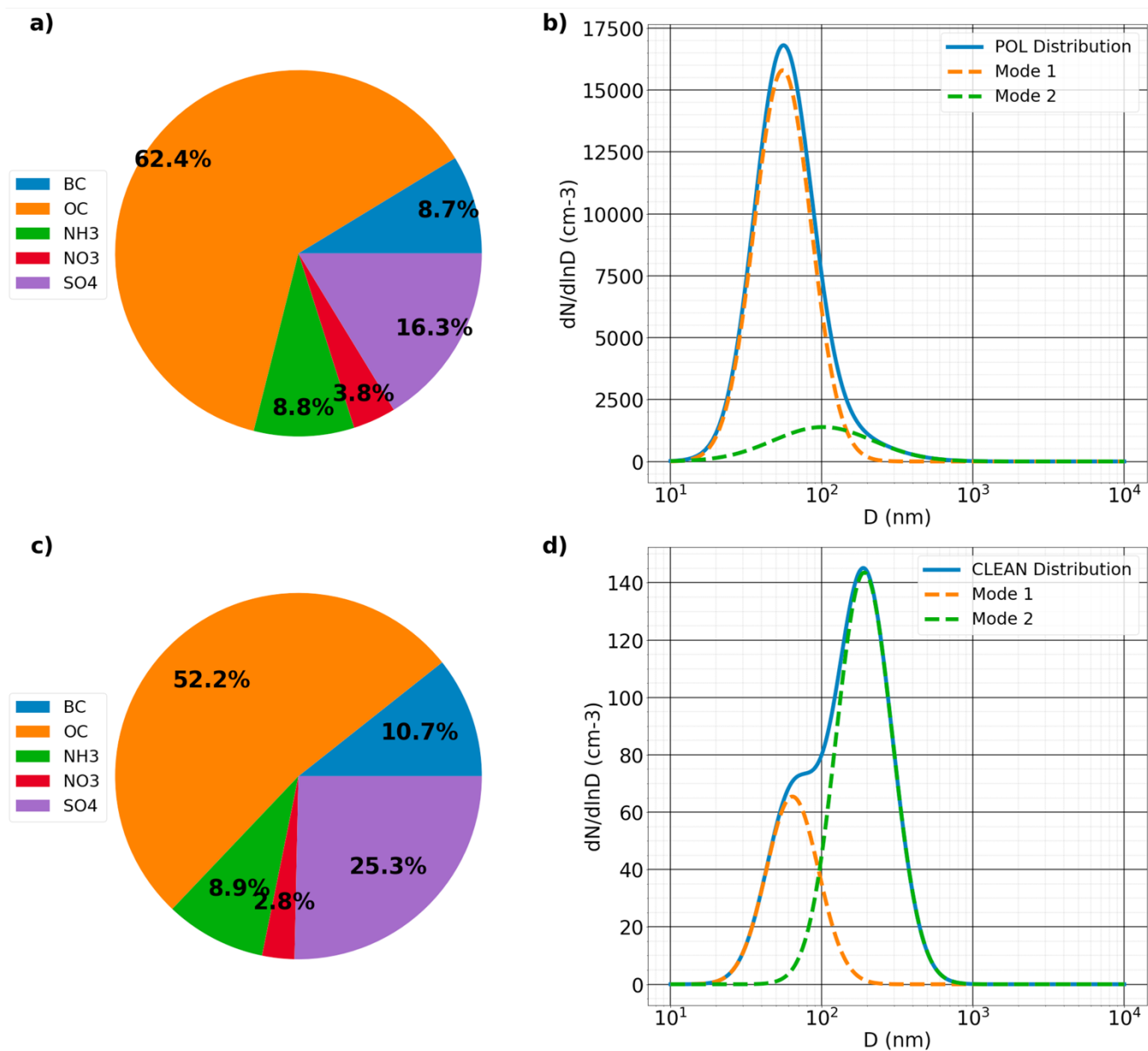
Acknowledgements. This study is supported by L'Agence National de la Recherche (ANR) of France under "Programme d'Investissements d'Avenir" (ANR-18-MPGA-003 EUROACE) and co-funded by University Toulouse III Paul Sabatier. The computation of this work was performed using HPC resources of French GENCI-IDRIS (Grant A0110110967 and A0090110967) and French Regional Computations center CALMIP. LD thanks the Laboratoire d'Aérodologie, Université de Toulouse, France, for funding and hosting his Ph.D. research activities. LD also thanks the MesoNH team, especially Quentin Rodier, Juan Escobar, and Philippe Wautelet, for their advises on using Meso-NH, Benoit Vié and Marie Mazoyer for their help to handle and modify microphysical scheme LIMA, Quentin Libois for explaining the details of Meso-NH's radiative schemes, and specifically Fabienne Lohou (LAERO) for her introduction of DACCIWA campaign alongside her guidance in using relevant data products. A special thanks the authors to all people whose work was involved in the measurement and processing of DACCIWA campaign data especially over the Savè supersite. Many constructive comments and suggestions from Dr. Mónica Zamora Zapata and an anonymous reviewer as well as the handling editor, Dr. Graham Feingold have made a substantial impact on our effort to improve the quality of the manuscript.

880

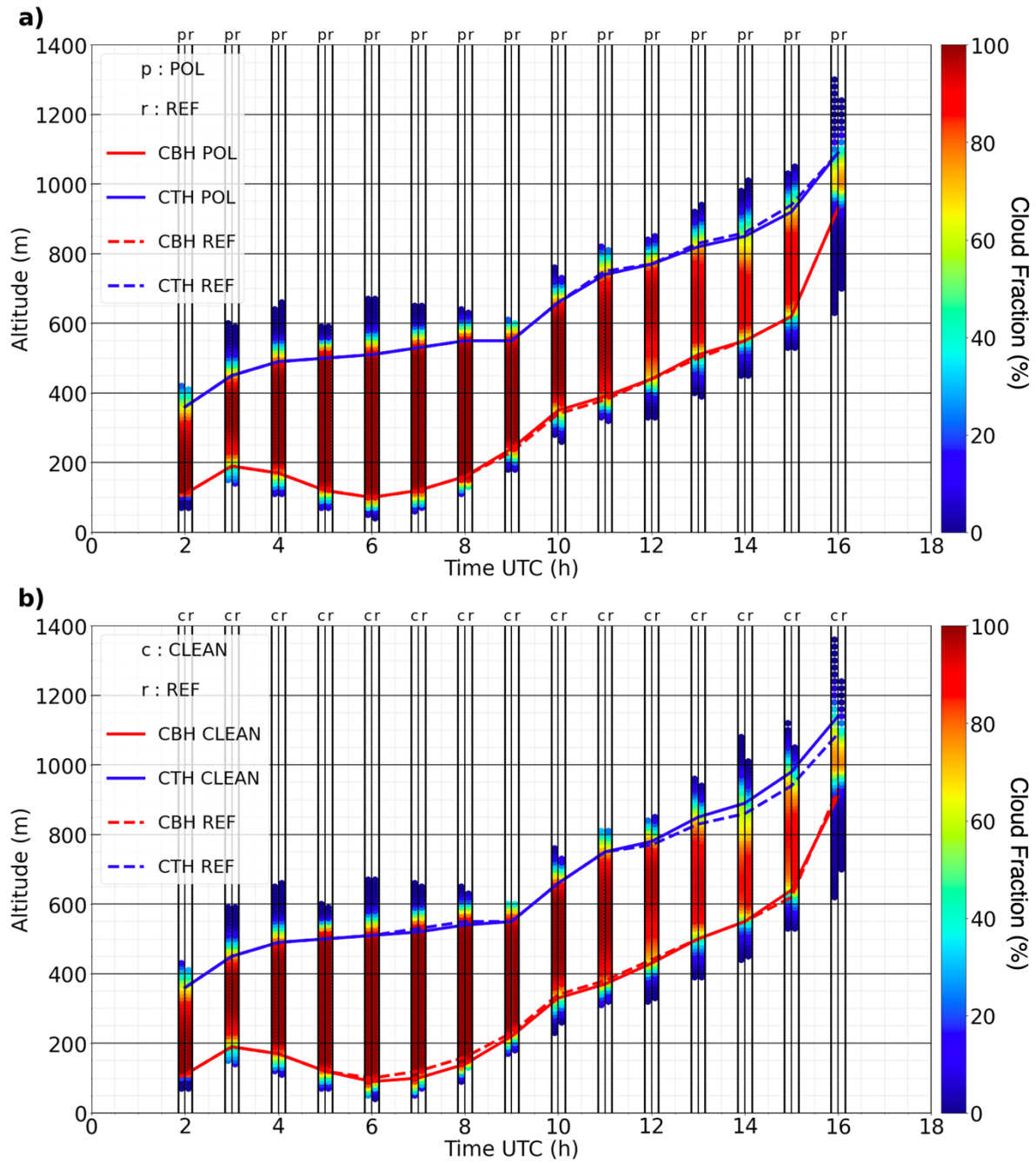
885

890

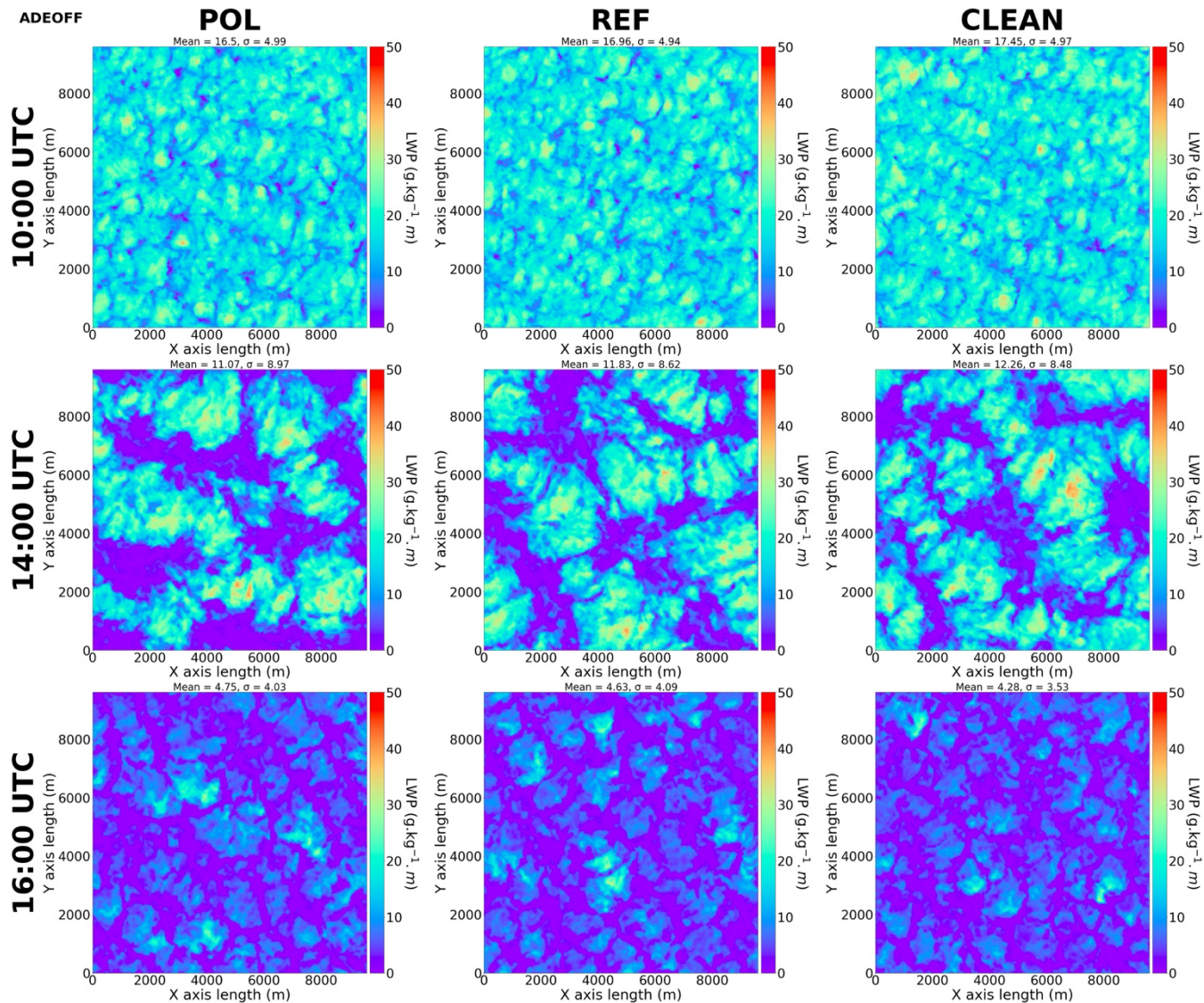
Appendix A



895 **Figure A1.** Mass composition (a,c) and size distribution provided by (Denjean et al., 2020a) and fitted into 2 modes described in Table 2 (b,d) for scenarios POL (top), CLEAN (bottom).



900 **Figure A2.** Mean LLSCs deck evolution of POL (a) and CLEAN (b) cases with the representation of REF's one to make comparison and REF_NOBC ADEON and ADEOFF runs (c), vertical color bars for POL/CLEAN (left) and REF (right) attribute at each altitude level a cloud presence density for both cases at each hour.



910 **Figure A3.** Liquid water path (LWP, $g\ kg^{-1}\ m$) in POL (left column), REF (mid-column), and CLEAN (right column) ADEOFF runs at 10:00 UTC (top row), 14:00 UTC (middle row), and 16:00 UTC (bottom row).

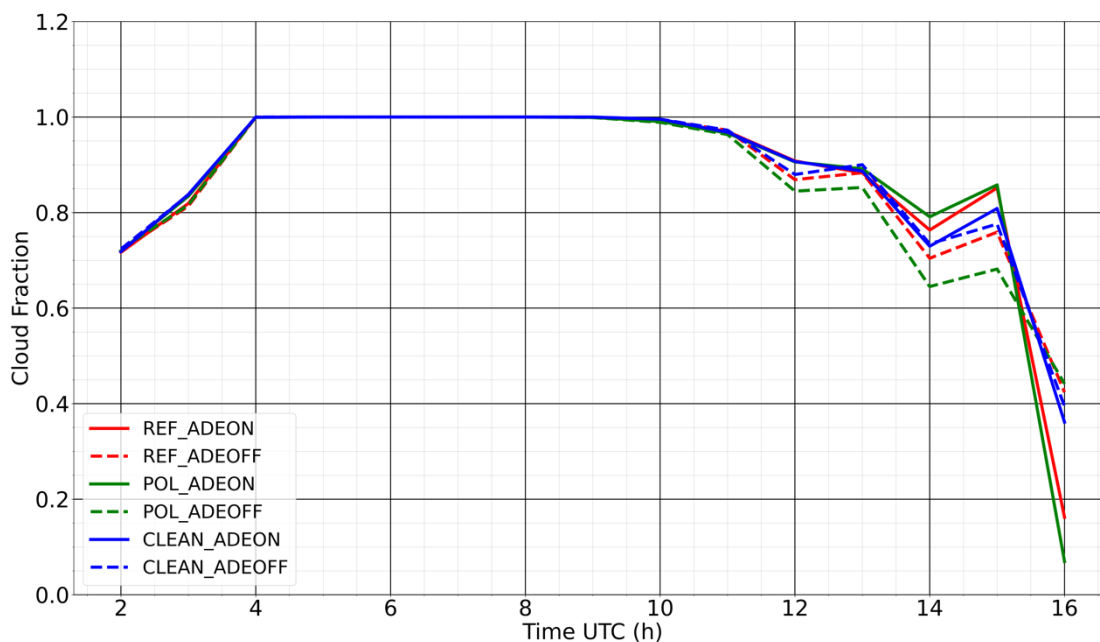


Figure A4. Domain averaged cloud fraction for AODON (solid lines) and AODOFF (dotted lines) of REF (red), POL (green), and CLEAN (blue) cases, derived using hourly model outputs. The cloud fraction here is a column quantity, defined as pixels where $LWP > 5 \text{ g kg}^{-1} \text{ m}$.

References

- Abdul-Razzak, H. and Ghan, S. J.: A parameterization of aerosol activation: 2. Multiple aerosol types, *J. Geophys. Res.-Atmos.*, 105, 6837–6844, <https://doi.org/10.1029/1999JD901161>, 2000.
- Abdul-Razzak, H. and Ghan, S. J.: Parameterization of the influence of organic surfactants on aerosol activation, *J. Geophys. Res.-Atmos.*, 109, <https://doi.org/10.1029/2003JD004043>, 2004.
- Ackerman, A. S., Kirkpatrick, M. P., Stevens, D. E., and Toon, O. B.: The impact of humidity above stratiform clouds on indirect aerosol climate forcing, *Nature*, 432, 1014–1017, <https://doi.org/10.1038/nature03174>, 2004.
- Adler, B., Babic, K., Kalthoff, N., Lohou, F., Lothon, M., Dione, C., Pedruzo-Bagazgoitia, X., and Andersen, H.: Nocturnal low-level clouds in the atmospheric boundary layer over southern West Africa: an observation-based analysis of conditions and processes, *Atmos. Chem. Phys.*, 19, 663–681, <https://doi.org/10.5194/acp-19-663-2019>, 2019.
- Aouizerats, B., Thouron, O., Tulet, P., Mallet, M., Gomes, L., and Henzing, J. S.: Development of an online radiative module for the computation of aerosol optical properties in 3-D atmospheric models: validation during the EUCAARI campaign, *Geoscientific Model Development*, 3, 553–564, <https://doi.org/10.5194/gmd-3-553-2010>, 2010.
- Babic, K., Adler, B., Kalthoff, N., Andersen, H., Dione, C., Lohou, F., Lothon, M., and Pedruzo-Bagazgoitia, X.: The observed diurnal cycle of low-level stratus clouds over southern West Africa: a case study, *Atmos. Chem. Phys.*, 19, 1281–1299, <https://doi.org/10.5194/acp-19-1281-2019>, 2019.
- Bauer, S. E., Im, U., Mezuman, K., and Gao, C. Y.: Desert Dust, Industrialization, and Agricultural Fires: Health Impacts of Outdoor Air Pollution in Africa, *J. Geophys. Res.-Atmos.*, 124, 4104–4120, <https://doi.org/10.1029/2018JD029336>, 2019.

- Bellon, G. and Stevens, B.: Time Scales of the Trade Wind Boundary Layer Adjustment, *J. Atmos. Sci.*, 70, 1071 – 1083, <https://doi.org/10.1175/JAS-D-12-0219.1>, 2013.
- 940 Boucher, O., D. Randall, P. Artaxo, C. Bretherton, G. Feingold, P. Forster, V.-M. Kerminen, Y. Kondo, H. Liao, U. Lohmann, P. Rasch, S.K. Satheesh, S. Sherwood, B. Stevens, and X.Y. Zhang: Clouds and Aerosols. In: Climate Change 2013: The Physical Science Basis. Contribution of Working Group I to the Fifth Assessment Report of the Intergovernmental Panel on Climate Change [Stocker, T.F., D. Qin, G.-K. Plattner, M. Tignor, S.K. Allen, J. Boschung, A. Nauels, Y. Xia, V. Bex and P.M. Midgley (eds.)]. Cambridge University Press, Cambridge, United Kingdom and New York, NY, USA, 2013.
- 945 Bretherton, C. S., Blossy, F. N., and Uchida, J. : Cloud droplet sedimentation, entrainment efficiency, and subtropical stratocumulus albedo, *Geophys. Res. Lett.*, 34, L03813, doi:10.1029/2006GL027648, 2007.
- Brito, J., Freney, E., Dominutti, P., Borbon, A., Haslett, S. L., Batenburg, A. M., Colomb, A., Dupuy, R., Denjean, C., Burnet, F., Bourriane, T., Deroubaix, A., Sellegri, K., Borrmann, S., Coe, H., Flamant, C., Knippertz, P., and Schwarzenboeck, A.: Assessing the role of anthropogenic and biogenic sources on PM₁ over southern West Africa using aircraft measurements, *Atmos. Chem. Phys.*, 18, 757–772, <https://doi.org/10.5194/acp-18-757-2018>, 2018.
- 950 Caniaux, G., Redelsperger, J.-L., and Lafore, J.-P.: A Numerical Study of the Stratiform Region of a Fast-Moving Squall Line. Part I: General Description and Water and Heat Budgets, *J. Atmos. Sci.*, 51, 2046 – 2074, [https://doi.org/10.1175/15200469\(1994\)051<2046:ANSOTS>2.0.CO;2](https://doi.org/10.1175/15200469(1994)051<2046:ANSOTS>2.0.CO;2), 1994.
- 955 Carslaw, K. S., Gordon, H., Hamilton, D. S., Johnson, J. S., Regayre, L. A., Yoshioka, M., and Pringle, K. J.: Aerosols in the Pre-industrial Atmosphere, *Current Climate Change Reports*, 3, 1–15, <https://doi.org/10.1007/s40641-017-0061-2>, 2017.
- Chatfield, R. B., Vastano, J. A., Li, L., Sachse, G. W., and Connors, V. S.: The Great African Plume from biomass burning: Generalizations from a three-dimensional study of TRACE A carbon monoxide, *J. Geophys. Res.-Atmos.*, 103, 28059–28077, <https://doi.org/https://doi.org/10.1029/97JD03363>, 1998.
- 960 Chen, T., Rossow, W. B., and Zhang, Y.: Radiative Effects of Cloud-Type Variations, *J. Clim.*, 13, 264 – 286, [https://doi.org/10.1175/1520-0442\(2000\)013<0264:REOCTV>2.0.CO;2](https://doi.org/10.1175/1520-0442(2000)013<0264:REOCTV>2.0.CO;2), 2000.
- Cleveland, W. S.: Robust Locally Weighted Regression and Smoothing Scatterplots, *Journal of the American Statistical Association*, 74, 829–836, <https://doi.org/10.1080/01621459.1979.10481038>, 1979.
- 965 Cohard, J.-M. and Pinty, J.-P.: A comprehensive two-moment warm microphysical bulk scheme. I: Description and tests, *Quar. J. Roy. Meteorol. Soc.*, 126, 1815–1842, <https://doi.org/https://doi.org/10.1002/qj.49712656613>, 2000.
- Dearden, C., Hill, A., Coe, H., and Choularton, T.: The role of droplet sedimentation in the evolution of low-level clouds over southern West Africa, *Atmos. Chem. Phys.*, 18, 14253–14269, <https://doi.org/10.5194/acp-18-14253-2018>, 2018.
- 970 Deetz, K., Vogel, H., Knippertz, P., Adler, B., Taylor, J., Coe, H., Bower, K., Haslett, S., Flynn, M., Dorsey, J., Crawford, I., Kottmeier, C., and Vogel, B.: Numerical simulations of aerosol radiative effects and their impact on clouds and atmospheric dynamics over southern West Africa, *Atmos. Chem. Phys.*, 18, 9767–9788, <https://doi.org/10.5194/acp-18-9767-2018>, 2018.
- 975 Denjean, C., Bourriane, T., Burnet, F., Mallet, M., Maury, N., Colomb, A., Dominutti, P., Brito, J., Dupuy, R., Sellegri, K., Schwarzenboeck, A., Flamant, C., and Knippertz, P.: Overview of aerosol optical properties over southern West Africa from DACCIIWA aircraft measurements, *Atmos. Chem. Phys.*, 20, 4735–4756, <https://doi.org/10.5194/acp-20-4735-2020>, 2020a.
- Denjean, C., Brito, J., Libois, Q., Mallet, M., Bourriane, T., Burnet, F., Dupuy, R., Flamant, C., and Knippertz, P.: Unexpected Biomass Burning Aerosol Absorption Enhancement Explained by Black Carbon Mixing State, *Geophys. Res. Lett.*, 47, e2020GL089055, <https://doi.org/https://doi.org/10.1029/2020GL089055>, e2020GL089055, 2020b.
- 980 Deroubaix, A., Menut, L., Flamant, C., Brito, J., Denjean, C., Dreiling, V., Fink, A., Jambert, C., Kalthoff, N., Knippertz, P., Ladkin, R., Mailler, S., Maranan, M., Pacifico, F., Pigué, B., Siour, G., and Turquety, S.: Diurnal cycle of coastal anthropogenic pollutant transport over southern West Africa during the DACCIIWA campaign, *Atmos. Chem. Phys.*, 19, 473–497, <https://doi.org/10.5194/acp-19-473-2019>, 2019.
- 985 Deroubaix, A., Menut, L., Flamant, C., Knippertz, P., Fink, A. H., Batenburg, A., Brito, J., Denjean, C., Dione, C., Dupuy, R., Hahn, V., Kalthoff, N., Lohou, F., Schwarzenboeck, A., Siour, G., Tuccella, P., and Voigt, C.: Sensitivity of low-

- level clouds and precipitation to anthropogenic aerosol emission in southern West Africa: a DACCIWA case study, *Atmos. Chem. Phys.*, 22, 3251–3273, <https://doi.org/10.5194/acp-22-3251-2022>, 2022.
- 990 Derrien, S., Bezombes, Y., Bret, B., Gabella, O., Jarnot, C., Medina, P., Piques, E., Delon, C., Dione, C., Campistron, B., Durand, P., Jambert, C., Lohou, F., Lothon, M., Pacifico, F., and Meyerfeld, Y.: DACCIWA field campaign, Savè super-site, UPS instrumentation, 10.6096/DACCIWA.1618, 2016.
- Dione, C., Lohou, F., Lothon, M., Adler, B., Babic, K., Kalthoff, N., Pedruzo-Bagazgoitia, X., Bezombes, Y., and Gabella, O.: Low-level stratiform clouds and dynamical features observed within the southern West African monsoon, *Atmos. Chem. Phys.*, 19, 8979–8997, <https://doi.org/10.5194/acp-19-8979-2019>, 2019.
- 995 Eastman, R. and Warren, S. G.: Diurnal Cycles of Cumulus, Cumulonimbus, Stratus, Stratocumulus, and Fog from Surface Observations over Land and Ocean, *J. Clim.*, 27, 2386 – 2404, <https://doi.org/10.1175/JCLI-D-13-00352.1>, 2014.
- Feingold, G., Jiang, H. L., and Harrington, J. Y.: On smoke suppression of clouds in Amazonia, *Geophys. Res. Lett.*, 32, 804, doi: 10.1029/2004GL021369, 2005.
- 1000 Flamant, C., Deroubaix, A., Chazette, P., Brito, J., Gaetani, M., Knippertz, P., Fink, A. H., de Coetlogon, G., Menut, L., Colomb, A., Denjean, C., Meynadier, R., Rosenberg, P., Dupuy, R., Dominutti, P., Duplissy, J., Bourriane, T., Schwarzenboeck, A., Ramonet, M., and Totems, J.: Aerosol distribution in the northern Gulf of Guinea: local anthropogenic sources, long-range transport, and the role of coastal shallow circulations, *Atmos. Chem. Phys.*, 18, 12363–12389, <https://doi.org/10.5194/acp-18-12363-2018>, 2018.
- Flossmann, A. I. and Wobrock, W.: Cloud Processing of Aerosol Particles in Marine Stratocumulus Clouds, *Atmosphere*, 10, <https://doi.org/10.3390/atmos10090520>, 2019.
- 1005 Fouquart, Y. and Bonnel, B.: Computations of solar heating of the earth’s atmosphere – A new parameterization, *Beitrag zur Physik der Atmosphäre*, 53, 35-62, 1980.
- Geoffroy, O., Brenguier, J.-L., and Sandu, I.: Relationship between drizzle rate, liquid water path and droplet concentration at the scale of a stratocumulus cloud system, *Atmos. Chem. Phys.*, 8, 4641–4654, <https://doi.org/10.5194/acp-8-4641-2008>, 2008.
- 1010 Ghonima, M., Heus, T., Norris, J. R., and J. Kleissl, J.: Factors controlling stratocumulus cloud lifetime over coastal land, *J. Atmos. Sci.*, 73, 2961-2983, 2016.
- Griffin, R. J., Nguyen, K., Dabdub, D., and Seinfeld, J. H.: A Coupled Hydrophobic-Hydrophilic Model for Predicting Secondary Organic Aerosol Formation, *J. Atmos. Chem.*, 44, 171–190, <https://doi.org/10.1023/A:1022436813699>, 2003.
- 1015 Hagan, H. D., Thompson, B., Palmo, J., and Ruskowski, A.: py-smps, <https://github.com/quant-aa/py-smps>, 2022.
- Handwerker, J., Scheer, S., and Gamer, T.: DACCIWA field campaign, Savè super-site, Cloud and precipitation, <https://doi.org/10.6096/daccciwa.1686>, 2016.
- Hannak, L., Knippertz, P., Fink, A. H., Kniffka, A., and Pante, G.: Why Do Global Climate Models Struggle to Represent Low-Level Clouds in the West African Summer Monsoon?, *J. Clim.*, 30, 1665 – 1687, <https://doi.org/10.1175/JCLI-D-16-0451.1>, 2017.
- 1020 Hansen, J., M. Sato, R. Ruedy, A. Lacis, and V. Oinas, Global warming in the twenty-first century: An alternative scenario. *PNAS*, 97, 9875-9880, 1998.
- Hartmann, D. L., Ockert-Bell, M. E., and Michelsen, M. L.: The Effect of Cloud Type on Earth’s Energy Balance: Global Analysis, *J. Clim.*, 5, 1281 – 1304, [https://doi.org/10.1175/1520-0442\(1992\)005<1281:TEOCTO>2.0.CO;2](https://doi.org/10.1175/1520-0442(1992)005<1281:TEOCTO>2.0.CO;2), 1992.
- 1025 Haslett, S. L., Taylor, J. W., Evans, M., Morris, E., Vogel, B., Dajuma, A., Brito, J., Batenburg, A. M., Borrmann, S., Schneider, J., Schulz, C., Denjean, C., Bourriane, T., Knippertz, P., Dupuy, R., Schwarzenböck, A., Sauer, D., Flamant, C., Dorsey, J., Crawford, I., and Coe, H.: Remote biomass burning dominates southern West African air pollution during the monsoon, *Atmos. Chem. Phys.*, 19, 15217–15234, <https://doi.org/10.5194/acp-19-15217-2019>, 2019.
- 1030 Haywood, J. and Boucher, O.: Estimates of the direct and indirect radiative forcing due to tropospheric aerosols: A review, *Rev. Geophys.*, 38, 513–543, <https://doi.org/10.1029/1999RG000078>, 2000.
- Hill, P. G., Allan, R. P., Chiu, J. C., Bodas-Salcedo, A., and Knippertz, P.: Quantifying the Contribution of Different Cloud Types to the Radiation Budget in Southern West Africa, *J. Clim.*, 31, 5273 – 5291, <https://doi.org/10.1175/JCLI-D-17-0586.1>, 2018.

- 1035 Huang, J., Wang, T., Wang, W., Li, Z., and Yan, H.: Climate effects of dust aerosols over East Asian arid and semiarid regions, *J. Geophys. Res.-Atmos.*, 119, 11,398–11,416, <https://doi.org/https://doi.org/10.1002/2014JD021796>, 2014.
- Jiang, G.-S. and Shu, C.-W.: Efficient Implementation of Weighted ENO Schemes, *J. Comp. Phys.*, 126, 202–228, <https://doi.org/https://doi.org/10.1006/jcph.1996.0130>, 1996.
- 1040 Jiang, H., Cotton, W. R., and Feingold, G.: Simulations of aerosol-cloud-dynamical feedbacks resulting from entrainment of aerosol into the marine boundary layer during the Atlantic Stratocumulus Transition Experiment, *J. Geophys. Res.*, 107, 4813, doi:10.1029/2001JD001502, 2002.
- Jiang, H., and Feingold, G.: Effect of aerosol on warm convective clouds: Aerosol-cloud-surface flux feedbacks in a new coupled large eddy model, *J. Geophys. Res.*, 111, doi:10.1029/2005JD006138, 2006.
- 1045 Johnson, B. T., Shine, K. P., and Forster, P. M.: The semi-direct aerosol effect: Impact of absorbing aerosols on marine stratocumulus, *Q. J. R. Meteorol. Soc.*, 130, 1407-1422, 2004.
- Kalthoff, N., Lohou, F., Brooks, B., Jegede, G., Adler, B., Babic, K., Dione, C., Ajao, A., Amekudzi, L. K., Aryee, J. N. A., Ay'oola, M., Bessardon, G., Danuor, S. K., Handwerker, J., Kohler, M., Lohou, M., Pedruzo-Bagazgoitia, X., Smith, V., Sunmonu, L., Wieser, A., Fink, A. H., and Knippertz, P.: An overview of the diurnal cycle of the atmospheric boundary layer during the West African monsoon season: results from the 2016 observational campaign, *Atmos. Chem. Phys.*, 18, 2913–2928, <https://doi.org/10.5194/acp-18-2913-2018>, 2018.
- 1050 Khairoutdinov, M. and Kogan, Y.: A New Cloud Physics Parameterization in a Large-Eddy Simulation Model of Marine Stratocumulus, *Mon. Weather Rev.*, 128, 229 – 243, [https://doi.org/10.1175/1520-0493\(2000\)128<0229:ANCPPI>2.0.CO;2](https://doi.org/10.1175/1520-0493(2000)128<0229:ANCPPI>2.0.CO;2), 2000.
- Knippertz, P., Fink, A. H., Schuster, R., Trentmann, J., Schrage, J. M., and Yorke, C.: Ultra-low clouds over the southern West African monsoon region, *Geophys. Res. Lett.*, 38, <https://doi.org/https://doi.org/10.1029/2011GL049278>, 2011.
- 1055 Knippertz, P., Coe, H., Chiu, J. C., Evans, M. J., Fink, A. H., Kalthoff, N., Liousse, C., Mari, C., Allan, R. P., Brooks, B., Danour, S., Flamant, C., Jegede, O. O., Lohou, F., and Marsham, J. H.: The DACCWA Project: Dynamics–Aerosol–Chemistry–Cloud Interactions in West Africa, *Bull. Amer. Meteor. Soc.*, 96, 1451 – 1460, <https://doi.org/10.1175/BAMS-D-14-00108.1>, 2015.
- 1060 Knippertz, P., Fink, A. H., Deroubaix, A., Morris, E., Tocquer, F., Evans, M. J., Flamant, C., Gaetani, M., Lavaysse, C., Mari, C., Marsham, J. H., Meynadier, R., Affo-Dogo, A., Bahaga, T., Brosse, F., Deetz, K., Guebsi, R., Latifou, I., Maranan, M., Rosenberg, P. D., and Schlueter, A.: A meteorological and chemical overview of the DACCWA field campaign in West Africa in June–July 2016, *Atmos. Chem. Phys.*, 17, 10893–10918, <https://doi.org/10.5194/acp-17-10893-2017>, 2017.
- 1065 Koch, D. and Del Genio, A. D.: Black carbon semi-direct effects on cloud cover: review and synthesis, *Atmos. Chem. Phys.*, 10, 7685–7696, <https://doi.org/10.5194/acp-10-7685-2010>, 2010a.
- Koch, D. and Del Genio, A. D.: Black carbon semi-direct effects on cloud cover: review and synthesis, *Atmos. Chem. Phys.*, 10, 7685–7696, <https://doi.org/10.5194/acp-10-7685-2010>, 2010b.
- 1070 Kreidenweis, S. M., Petters, M., and Lohmann, U.: 100 Years of Progress in Cloud Physics, Aerosols, and Aerosol Chemistry Research, *Meteorological Monographs*, 59, 11.1 – 11.72, <https://doi.org/10.1175/AMSMONOGRAPHS-D-18-0024.1>, 2019.
- Lac, C., Chaboureau, J.-P., Masson, V., Pinty, J.-P., Tulet, P., Escobar, J., Leriche, M., Barthe, C., Aouizerats, B., Augros, C., Aumond, P., Auguste, F., Bechtold, P., Berthet, S., Bielli, S., Bosseur, F., Caumont, O., Cohard, J.-M., Colin, J., Couvreux, F., Cuxart, J., Delautier, G., Dauhut, T., Ducrocq, V., Filippi, J.-B., Gazen, D., Geoffroy, O., Gheusi, F., Honnert, R., Lafore, J.-P., Lebeau-pin Brossier, C., Libois, Q., Lunet, T., Mari, C., Maric, T., Mascart, P., Mogé, M., Molinié, G., Nuissier, O., Pantillon, F., Peyrillé, P., Pergaud, J., Perraud, E., Pianezze, J., Redelsperger, J.-L., Ricard, D., Richard, E., Riette, S., Rodier, Q., Schoetter, R., Seyfried, L., Stein, J., Suhre, K., Taufour, M., Thouron, O., Turner, S., Verrelle, A., Vié, B., Visentin, F., Vionnet, V., and Wautelet, P.: Overview of the Meso-NH model version 5.4 and its applications, *Geoscientific Model Development*, 11, 1929–1969, <https://doi.org/10.5194/gmd-11-1929-2018>, 2018.
- 1080 Lunet, T., Lac, C., Auguste, F., Visentin, F., Masson, V., and Escobar, J.: Combination of WENO and Explicit Runge- Kutta methods for wind transport in Meso-NH model, *Mon. Weather Rev.*, 145, 3817–3838, <https://doi.org/10.1175/MWR-D616-0343.12017>, 2017.

- 1085 Lascaux, F., Richard, E., and Pinty, J.-P.: Numerical simulations of three different MAP IOPs and the associated microphysical processes, *Quart. J. Roy. Meteorol. Soc.*, 132, 1907–1926, <https://doi.org/https://doi.org/10.1256/qj.05.197>, 2006.
- Legain, D., Bousquet, O., Douffet, T., Tzanos, D., Moulin, E., Barrie, J., and Renard, J.-B.: High-frequency boundary layer profiling with reusable radiosondes, *Atmospheric Measurement Techniques*, 6, 2195–2205, <https://doi.org/10.5194/amt-6-2195-2013>, 2013.
- 1090 Li, J., Carlson, B. E., Yung, Y. L., Lv, D., Hansen, J., Penner, J. E., Liao, H., Ramaswamy, V., Kahn, R. A., Zhang, P., Dubovik, O., Ding, A., Laciš, A. A., Zhang, L., and Dong, Y.: Scattering and absorbing aerosols in the climate system, *Nature Reviews Earth & Environment*, 3, 363–379, <https://doi.org/10.1038/s43017-022-00296-7>, 2022.
- Lioussé, C., Assamoi, E., Criqui, P., Granier, C., and Rosset, R.: Explosive growth in African combustion emissions from 2005 to 2030, *Environ. Res. Lett.*, 9, 035003, <https://doi.org/10.1088/1748-9326/9/3/035003>, 2014.
- 1095 Liu, Y., Jia, R., Dai, T., Xie, Y., and Shi, G.: A review of aerosol optical properties and radiative effects, *Journal of Meteorological Research*, 28, 1003–1028, <https://doi.org/10.1007/s13351-014-4045-z>, 2014.
- Lohmann, U. and Feichter, J.: Can the direct and semi-direct aerosol effect compete with the indirect effect on a global scale?, *Geophys. Res. Lett.*, 28, 159–161, <https://doi.org/https://doi.org/10.1029/2000GL012051>, 2001.
- Lohou, F., Kalthoff, N., Adler, B., Babic, K., Dione, C., Lathon, M., Pedruzo-Bagazgoitia, X., and Zouzoua, M.: Conceptual model of diurnal cycle of low-level stratiform clouds over southern West Africa, *Atmos. Chem. Phys.*, 20, 2263–2275, <https://doi.org/10.5194/acp-20-2263-2020>, 2020.
- Mari, C., Evans, M. J., Palmer, P. I., Jacob, D. J., and Sachse, G. W.: Export of Asian pollution during two cold front episodes of the TRACE-P experiment, *J. Geophys. Res.-Atmos.*, 109, <https://doi.org/https://doi.org/10.1029/2003JD004307>, 2004.
- 1105 Mari, C. H., Cailley, G., Corre, L., Saunois, M., Attié, J. L., Thouret, V., and Stohl, A.: Tracing biomass burning plumes from the Southern Hemisphere during the AMMA 2006 wet season experiment, *Atmos. Chem. Phys.*, 8, 3951–3961, <https://doi.org/10.5194/acp-8-3951-2008>, 2008.
- Marticorena, B. and Bergametti, G.: Two-year simulations of seasonal and interannual changes of the Saharan dust emissions, *Geophys. Res. Lett.*, 23, 1921–1924, <https://doi.org/https://doi.org/10.1029/96GL01432>, 1996.
- 1110 Martin, G. M., Johnson, D. W., and Spice, A.: The Measurement and Parameterization of Effective Radius of Droplets in Warm Stratocumulus Clouds, *J. Atmos. Sci.*, 51, 1823 – 1842, [https://doi.org/10.1175/15200469\(1994\)051<1823:TMAPOE>2.0.CO;2](https://doi.org/10.1175/15200469(1994)051<1823:TMAPOE>2.0.CO;2), 1994.
- Masson, V., Le Moigne, P., Martin, E., Faroux, S., Alias, A., Alkama, R., Belamari, S., Barbu, A., Boone, A., Bouyssel, F., Brousseau, P., Brun, E., Calvet, J.-C., Carrer, D., Decharme, B., Delire, C., Donier, S., Essaouini, K., Gibelin, A.-L., 1115 Giordani, H., Habets, F., Jidane, M., Kerdraon, G., Kourzeneva, E., Lafaysse, M., Lafont, S., Lebeaupin Brossier, C., Lemonsu, A., Mahfouf, J.-F., Marguinaud, P., Mokhtari, M., Morin, S., Pigeon, G., Salgado, R., Seity, Y., Taillefer, F., Tanguy, G., Tulet, P., Vincendon, B., Vionnet, V., and Voldoire, A.: The SURFEXv7.2 land and ocean surface platform for coupled or offline simulation of earth surface variables and fluxes, *Geoscientific Model Development*, 6, 929–960, <https://doi.org/10.5194/gmd-6-929-2013>, 2013.
- 1120 Menut, L., Flamant, C., Turquety, S., Deroubaix, A., Chazette, P., and Meynadier, R.: Impact of biomass burning on pollutant surface concentrations in megacities of the Gulf of Guinea, *Atmos. Chem. Phys.*, 18, 2687–2707, <https://doi.org/10.5194/acp18-2687-2018>, 2018.
- Menut, L., Tuccella, P., Flamant, C., Deroubaix, A., and Gaetani, M.: The role of aerosol–radiation–cloud interactions in linking anthropogenic pollution over southern west Africa and dust emission over the Sahara, *Atmos. Chem. Phys.*, 19, 14657–14676, <https://doi.org/10.5194/acp-19-14657-2019>, 2019.
- 1125 Metzger, S., Dentener, F., Pandis, S., and Lelieveld, J.: Gas/aerosol partitioning: 1. A computationally efficient model, *J. Geophys. Res.-Atmos.*, 107, ACH 16–1–ACH 16–24, <https://doi.org/https://doi.org/10.1029/2001JD001102>, 2002.
- Mlawer, E. J., Taubman, S. J., Brown, P. D., Iacono, M. J., and Clough, S. A.: Radiative transfer for inhomogeneous atmospheres: RRTM, a validated correlated-k model for the longwave, *J. Geophys. Res.-Atmos.*, 102, 16663–16682, 1130 <https://doi.org/https://doi.org/10.1029/97JD00237>, 1997.
- Morcrette, J.-J.: The Surface Downward Longwave Radiation in the ECMWF Forecast System, *J. Clim.*, 15, 1875 – 1892, [https://doi.org/10.1175/1520-0442\(2002\)015<1875:TSDLRI>2.0.CO;2](https://doi.org/10.1175/1520-0442(2002)015<1875:TSDLRI>2.0.CO;2), 2002.

- Murphy, J. G., Oram, D. E., and Reeves, C. E.: Measurements of volatile organic compounds over West Africa, *Atmos. Chem. Phys.*, 10, 5281–5294, <https://doi.org/10.5194/acp-10-5281-2010>, 2010.
- 1135 Noilhan, J. and Planton, S.: A Simple Parameterization of Land Surface Processes for Meteorological Models, *Mon. Weather Rev.*, 117, 536 – 549, [https://doi.org/10.1175/1520-0493\(1989\)117<0536:ASPOLS>2.0.CO;2](https://doi.org/10.1175/1520-0493(1989)117<0536:ASPOLS>2.0.CO;2), 1989.
- Pedruzo-Bagazgoitia, X., de Roode, S. R., Adler, B., Babic, K., Dione, C., Kalthoff, N., Lohou, F., Lothon, M., and Vilà-Guerau de Arellano, J.: The diurnal stratocumulus-to-cumulus transition over land in southern West Africa, *Atmos. Chem. Phys.*, 20, 2735–2754, <https://doi.org/10.5194/acp-20-2735-2020>, 2020.
- 1140 Pinty, J.-P. and Jabouille, P.: A mixed-phased cloud parameterization for use in a mesoscale non-hydrostatic model: simulations of a squall line and of orographic precipitation, *Proc. Conf. on Cloud Physics*, 217–220. 1998.
- Pruppacher, H. R., Klett, J. D., and Wang, P. K.: Microphysics of Clouds and Precipitation, *Aerosol Science and Technology*, 28, 381–382, <https://doi.org/10.1080/02786829808965531>, 1998.
- 1145 Reeves, C. E., Formenti, P., Afif, C., Ancellet, G., Attié, J.-L., Bechara, J., Borbon, A., Cairo, F., Coe, H., Crumeyrolle, S., Fierli, F., Flamant, C., Gomes, L., Hamburger, T., Lambert, C., Law, K. S., Mari, C., Jones, R. L., Matsuki, A., Mead, M. I., Methven, J., Mills, G. P., Minikin, A., Murphy, J. G., Nielsen, J. K., Oram, D. E., Parker, D. J., Richter, A., Schlager, H., Schwarzenboeck, A., and Thouret, V.: Chemical and aerosol characterisation of the troposphere over West Africa during the monsoon period as part of AMMA, *Atmos. Chem. Phys.*, 10, 7575–7601, <https://doi.org/10.5194/acp-10-7575-2010>, 2010.
- 1150 Sandu, I., Brenguier, J.-L., Geoffroy, O., Thouron, O., and Masson, V.: Aerosol Impacts on the Diurnal Cycle of Marine Stratocumulus, *J. Atmos. Sci.*, 65, 2705 – 2718, <https://doi.org/10.1175/2008JAS2451.1>, 2008.
- Sauvage, B., Thouret, V., Cammas, J.-P., Gheusi, F., Athier, G., and Nédélec, P.: Tropospheric ozone over Equatorial Africa: regional aspects from the MOZAIC data, *Atmos. Chem. Phys.*, 5, 311–335, <https://doi.org/10.5194/acp-5-311-2005>, 2005.
- 1155 Schrage, J. M. and Fink, A. H.: Nocturnal Continental Low-Level Stratus over Tropical West Africa: Observations and Possible Mechanisms Controlling Its Onset, *Mon. Weather Rev.*, 140, 1794 – 1809, <https://doi.org/10.1175/MWR-D-11-00172.1>, 2012.
- Schuster, R., Fink, A. H., and Knippertz, P.: Formation and maintenance of nocturnal low-level stratus over the Southern West African monsoon region during AMMA 2006, *J. Atmos. Sci.*, 70, 2337 – 2355, <https://doi.org/10.1175/JAS-D-120241.1>, 2013.
- 1160 Stevens, B., Cotton, W. R., Feingold, G., and Moeng, C.-H.: Large-eddy simulations of strongly precipitating, shallow, stratocumulus-topped boundary layers, *J. Atmos. Sci.*, 55, 3616–3638, 1998.
- Stevens, B., Moeng, C.-H., Ackerman, A. S., Bretherton, C. S., Chlond, A., de Roode, S., Edwards, J., Golaz, J.-C., Jiang, H., Khairoutdinov, M., Kirkpatrick, M. P., Lewellen, D. C., Lock, A., Müller, F., Stevens, D. E., Whelan, E., and Zhu, P.: Evaluation of large-eddy simulations via observations of nocturnal marine stratocumulus, *Mon. Weather Rev.*, 133, 1443–1462, <https://doi.org/10.1175/MWR2930.1>, 2005.
- 1165 Stjern, C. W., Samset, B. H., Myhre, G., Forster, P. M., Hodnebrog, , Andrews, T., Boucher, O., Faluvegi, G., Iversen, T., Kasoar, M., Kharin, V., Kirkevåg, A., Lamarque, J.-F., Olivie, D., Richardson, T., Shawki, D., Shindell, D., Smith, C. J., Takemura, T., and Voulgarakis, A.: Rapid adjustments cause weak surface temperature response to increased black carbon concentrations, *J. Geophys. Res.-Atmos.*, 122, 11,462–11,481, <https://doi.org/https://doi.org/10.1002/2017JD027326>, 2017.
- 1170 Taylor, J. W., Haslett, S. L., Bower, K., Flynn, M., Crawford, I., Dorsey, J., Choulaton, T., Connolly, P. J., Hahn, V., Voigt, C., Sauer, D., Dupuy, R., Brito, J., Schwarzenboeck, A., Bourriane, T., Denjean, C., Rosenberg, P., Flamant, C., Lee, J. D., Vaughan, A. R., Hill, P. G., Brooks, B., Catoire, V., Knippertz, P., and Coe, H.: Aerosol influences on low-level clouds in the West African monsoon, *Atmos. Chem. Phys.*, 19, 8503–8522, <https://doi.org/10.5194/acp-19-8503-2019>, 2019.
- 1175 Thouron, O., Brenguier, J.-L., and Burnet, F.: Supersaturation calculation in large eddy simulation models for prediction of the droplet number concentration, *Geoscientific Model Development*, 5, 761–772, <https://doi.org/10.5194/gmd-5-761-2012>, 2012.

- 1180 Tulet, P., Crassier, V., Solmon, F., Guedalia, D., and Rosset, R.: Description of the mesoscale nonhydrostatic chemistry model and application to a transboundary pollution episode between northern France and southern England, *J. Geophys. Res.-Atmos.*, 108, ACH 5–1–ACH 5–11, <https://doi.org/https://doi.org/10.1029/2000JD000301>, 2003.
- Tulet, P., Crassier, V., Cousin, F., Suhre, K., and Rosset, R.: ORILAM, a three-moment lognormal aerosol scheme for mesoscale atmospheric model: Online coupling into the Meso-NH-C model and validation on the Escompte campaign, *J. Geophys. Res.-Atmos.*, 110, <https://doi.org/10.1029/2004JD005716>, 2005.
- 1185 Tulet, P., Grini, A., Griffin, R. J., and Petitcol, S.: ORILAM-SOA: A computationally efficient model for predicting secondary organic aerosols in three-dimensional atmospheric models, *J. Geophys. Res.-Atmos.*, 111, <https://doi.org/10.1029/2006JD007152>, 2006.
- Twohy, C. H., Anderson, J. R., Toohey, D. W., Andrejczuk, M., Adams, A., Lytle, M., George, R. C., Wood, R., Saide, P., Spak, S., Zuidema, P., and Leon, D.: Impacts of aerosol particles on the microphysical and radiative properties of stratocumulus clouds over the southeast Pacific Ocean, *Atmos. Chem. Phys.*, 13, 2541–2562, <https://doi.org/10.5194/acp-13-2541-2013>, 2013.
- 1190 Twomey, S.: PRECIPITATION BY DIRECT INTERCEPTION OF CLOUD-WATER, *Weather*, 12, 120–122, <https://doi.org/https://doi.org/10.1002/j.1477-8696.1957.tb00453.x>, 1957.
- 1195 Van der Dussen, J. J., de Roode, S. R., and Siebesma, A. P.: Factors controlling rapid stratocumulus cloud thinning, *J. Atmos. Sci.*, 71, 655–664, <https://doi.org/10.1175/JAS-D-13-0114.1>, 2014.
- Vié, B., Pinty, J.-P., Berthet, S., and Leriche, M.: LIMA (v1.0): A quasi two-moment microphysical scheme driven by a multimodal population of cloud condensation and ice freezing nuclei, *Geoscientific Model Development*, 9, 567–586, <https://doi.org/10.5194/gmd-9-567-2016>, 2016.
- 1200 Wang, S., Wang, Q., and Feingold, G.: Turbulence, Condensation, and Liquid Water Transport in Numerically Simulated Nonprecipitating Stratocumulus Clouds, *J. Atmos. Sci.*, 60, 262–278, [https://doi.org/10.1175/1520-0469\(2003\)060<0262:TCALWT>2.0.CO;2](https://doi.org/10.1175/1520-0469(2003)060<0262:TCALWT>2.0.CO;2), 2003.
- Wood, R.: Stratocumulus Clouds, *Mon. Weather Rev.*, 140, 2373 – 2423, <https://doi.org/10.1175/MWR-D-11-00121.1>, 2012.
- 1205 Yamaguchi, T., Feingold, G., Kazil, J., and McComiskey, A.: Stratocumulus to cumulus transition in the presence of elevated smoke layers, *Geophys. Res. Lett.*, 42, 10,478–10,485, <https://doi.org/https://doi.org/10.1002/2015GL066544>, 2015.
- Zhang, J. and Zuidema, P.: The diurnal cycle of the smoky marine boundary layer observed during August in the remote southeast Atlantic, *Atmos. Chem. Phys.*, 19, 14493–14516, <https://doi.org/10.5194/acp-19-14493-2019>, 2019.
- 1210 Zouzoua, M., Lohou, F., Assamoi, P., Lothon, M., Yoboue, V., Dione, C., Kalthoff, N., Adler, B., Babic, K., Pedruzo-Bagazgoitia, X., and Derrien, S.: Breakup of nocturnal low-level stratiform clouds during the southern West African monsoon season, *Atmos. Chem. Phys.*, 21, 2027–2051, <https://doi.org/10.5194/acp-21-2027-2021>, 2021.